Middle Carboniferous crustal melting in the Variscan Belt: New insights from U-Th-Pbtot. monazite and U-Pb zircon ages of the Montagne Noire Axial Zone (southern French Massif Central)

Michel Faure, Alain Cocherie, Eugène Be Mezeme, Nicolas Charles, Philippe Rossi

Middle Carboniferous crustal melting in the Variscan Belt: New insights from U–Th–$Pb_{tot.}$ monazite and U–Pb zircon ages of the Montagne Noire Axial Zone (southern French Massif Central)

Michel Faure[a], Alain Cocherie[b], Eugène Bé Mézème[a b], Nicolas Charles[a] and Philippe Rossi[b]

[a] Université d'Orléans-CNRS/INSU, Institut des Sciences de la Terre d'Orléans (ISTO), Campus Géosciences, 1A Rue de la Férollerie 45071 Orléans Cedex 2, France

[b] BRGM, Av. Claude-Guillemin, BP 36009, 45060 Orléans Cedex 2, France

Abstract

In France, the Devonian–Carboniferous Variscan orogeny developed at the expense of continental crust belonging to the northern margin of Gondwana. A Visean–Serpukhovian crustal melting has been recently documented in several massifs. However, in the Montagne Noire of the Variscan French Massif Central, which is the largest area involved in this partial melting episode, the age of migmatization was not clearly settled. Eleven U–Th–$Pb_{tot.}$ ages on monazite and three U–Pb ages on associated zircon are reported from migmatites (La Salvetat, Ourtigas), anatectic granitoids (Laouzas, Montalet) and post-migmatitic granites (Anglès, Vialais, Soulié) from the Montagne Noire Axial Zone are presented here for the first time. Migmatization and emplacement of anatectic granitoids took place around 333–326 Ma (Visean) and late granitoids emplaced around 325–318 Ma (Serpukhovian). Inherited zircons and monazite date the orthogneiss source rock of the Late Visean melts between 560 Ma and 480 Ma. In migmatites and anatectic granites, inherited crystals dominate the zircon populations. The migmatitization is the middle crust expression of a pervasive Visean crustal melting event also represented by the "Tufs anthracifères" volcanism in the northern Massif Central. This crustal melting is widespread in the French Variscan belt, though it is restricted to the upper plate of the collision belt. A mantle input appears as a likely mechanism to release the heat necessary to trigger the melting of the Variscan middle crust at a continental scale.

Keywords: Migmatites; U–Th–Pb chemical dating; U–Pb geochronology; Variscan Belt; French Massif Central

1. Introduction

Crustal melting is a common phenomenon observed in many collision belts, such as Himalaya, Variscan, Appalachian, Qinling–Dabie–Sulu, etc. This feature is often interpreted as the response to thermal relaxation during syn-, or late-collisional unthickening of previously thickened continental crust (e.g. [Le Fort, 1981], [Harris & Massey, 1994], [Faure et al., 2003], [Guillot et al., 2003], [Whitney et al., 2004], [Brown, 2005] and [Faure et al., 2008]).

The Variscan Belt of Western and Central Europe is a Paleozoic collisional orogen that involved large continental masses, such as Gondwana, Baltica and Laurussia, and several

Gondwana-derived microcontinents, such as Avalonia, Armorica, Mid-German Crystalline Rise (e.g. [Paris & Robardet, 1990], [Matte, 1991], [Tait et al., 1997], [Franke, 2000], [Matte, 2001], [Von Raumer et al., 2009], [Johnston & Gutierrez-Alonso, 2010], [Melleton et al., 2010a] and [Melleton et al., 2010b]). The detail paleogeographic and geodynamic reconstructions of the Variscan Belt remain controversial, nevertheless, there is a wide agreement that most of continent amalgamation was completed in the Early Carboniferous. Since the Late Visean, intracontinental deformation, namely wrenching, thrusting and normal faulting was coeval with intense crustal melting. However, the timing and tectonic setting of these late-collisional events is not clearly settled yet. This paper deals with age constraints on the Middle Carboniferous (Visean) migmatites and granitoids exposed in the Axial Zone of the Montagne Noire in the southern French Massif Central. New U–Th–$Pb_{tot.}$ ages on monazite using Electron Probe Microanalyzer (EPMA) method and U–Pb ages on zircon using High Resolution Secondary Ion Mass Spectrometry (HR-SIMS) were determined to date migmatites, anatectic granitoids and late to post-migmatitic granitic plutons are provided. These data are combined with the available ages of crustal melting known in other Middle Carboniferous migmatitic complexes recognized in the French Massif Central, Massif Armoricain, Vosges and Variscan Pyrénées. A possible geodynamic interpretation of the crustal melting experienced by this segment of the Variscan Belt is discussed.

2. An outline of the Variscan French Massif Central

It is now well accepted that the French Massif Central, which is one of the largest pieces of the Variscan belt of Western Europe, belongs entirely to the northern Gondwana margin. Its bulk architecture results of the stacking of several tectonic–metamorphic units. From bottom to top, and from South to North, five main tectonic–metamorphic units are recognized, namely (Fig. 1): 1) the late Visean foreland basin; 2) the fold-and-thrust belt; 3) the para-autochthonous unit; 4) the Lower Gneiss Unit; 5) the Upper Gneiss Unit (for detail, see [Faure et al., 2005] and [Faure et al., 2009a] and enclosed references).

The French Massif Central experienced several tectonic–metamorphic events (e.g. [Pin & Peucat, 1986], [Ledru et al., 1989], [Faure et al., 1997], [Faure et al., 2005], [Faure et al., 2009a] and [Faure et al., 2009b]). From Late Silurian to Middle Devonian, the northward continental subduction of the Gondwana margin beneath the Armorica microplate is coeval with the formation of high (or ultra-high) pressure rocks, called D0 event (Lardeaux et al., 2001). Around 380 Ma, the D1 event, referred to as the Eo-Variscan event, is responsible for nappe stacking, exhumation of the high-pressure rocks and the first crustal melting (cf. Faure et al, 2008 and enclosed references). A NE–SW-trending stretching lineation associated with a top-to-the-SW shearing develops during D1 (Roig and Faure, 2000). The stack of nappes is reworked by a D2 event, dated around 360–350 Ma (Late Devonian to Early Carboniferous), and characterized by a top-to-the NW shearing, and coeval with an intermediate pressure–temperature metamorphism ([Roig & Faure, 2000], [Bellot, 2001], [Duguet et al., 2007] and [Melleton et al., 2009]). A Middle Carboniferous thrusting event, called D3, and dated at 340–330 Ma, characterized by South to SW-directed ductile shearing develops only in the southern part of the French Massif Central (e.g. [Arthaud & Matte, 1977], [Ledru et al., 1989] and [Faure et al., 2005]). At the same time, in the northern part of the Massif, the onset of the syn-orogenic extension took place. During the early Late Carboniferous times, around 320–310 Ma, the entire belt experienced extensional tectonics characterized by a pervasive NW–SE striking stretching well recorded by the architecture and emplacement mechanisms of the syn-kinematic granitoids (Faure, 1995).

The French Massif Central exhibits a large amount of magmatic rocks (e. g. [Duthou et al., 1984] and [Pin & Duthou, 1990] and enclosed references). The pre-orogenic Early Paleozoic (mainly Early Cambrian and Early Ordovician) and the Devonian–Early Carboniferous magmatic stages are not presented here (for detail, see Faure et al., 2005 and enclosed references). Since the Middle Carboniferous D3 event, several episodes of crustal melting are recognized. The Late Visean magmatism (ca. 330 Ma), which is represented by the volcanic and sedimentary "Tufs anthracifères" series, is restricted to the northern part of the French Massif Central (Fig. 1). There, rhyolitic to dacitic dykes, microgranites and porphyritic granites represent deeper occurrences of the Late Visean crustal melting event (Faure et al., 2002). During the early Late Carboniferous (Serpukhovian to Baskirian, ca 325 Ma to 310 Ma), crustal melting is represented by a large amount of granitic intrusions. As noticed for a long time (e.g. Didier and Lameyre, 1969), two-mica leucogranites and porphyritic monzogranites are widespread in the northwestern and southeastern parts of the Massif Central, respectively; nevertheless, both types of plutons emplaced in an extensional tectonic setting. Lastly, at the end of the Carboniferous (Moscovian to Gzhelian, 310–300 Ma), cordierite anatectic granite is coeval with the Velay migmatitic event. Furthermore, alkaline acidic and intermediate volcanic rocks emplaced within the intramontane coal basins.

Three generations of migmatites are also recognized during the Paleozoic evolution of the French Massif Central. The oldest one develops from Middle to Late Devonian (ca. 390 to 375 Ma). This Eo-Variscan crustal melting stage is related to the exhumation of the high-pressure metamorphic rocks during the D1 event under ca 600 °C–10 kbar and 800 °C–7 kbar ([Pin & Peucat, 1986] and [Faure et al., 2008]). The second generation of migmatites crops out in the North Cévennes, South Millevaches, and Montagne Noire Axial Zone (Fig. 1). Recent U–Th–$Pb_{tot.}$ monazite ages in the North Cévennes and South Millevaches range around 330–326 Ma and 337–328 Ma, respectively ([Bé Mézème et al., 2006] and [Faure et al., 2009b]). The third generation of migmatite, dated of Late Carboniferous (ca. 300 Ma) is observed only in the Velay dome (Ledru et al., 2001). Among the Visean migmatites, the Montagne Noire Axial Zone is the largest area. However, there the age of the crustal melting was poorly constrained by the age of the late migmatitic plutons ([Hamet & Allègre, 1976] and [Matte et al., 1998]). In the following, new U–Th–Pb monazite and U–Pb zircon single grain ages for the migmatites, the related anatectic granitoids, and the late migmatitic leucogranites that crop out in the Axial Zone of the Montagne Noire are provided.

3. Geological setting of the Montagne Noire

Conversely to the northern part of the French Massif Central, in the southern area, the Devonian tectono-metamorphic events (D0 and D1) are lacking. The Montagne Noire underwent its first deformation during the Middle Carboniferous, from Visean to Serpukhovian (early Namurian). Since (Gèze, 1949) and (Arthaud, 1970), the Montagne Noire is classically subdivided from south to north in southern, axial and northern zones ([Fig. 1] and [Fig. 2]). The Paleozoic series consist of sedimentary rocks ranging from Early Cambrian to Silurian and from early Cambrian to Visean in the northern and southern zones, respectively. These series are involved into kilometre-sized, south verging recumbent folds. The age of the recumbent folding is stratigraphically constrained by the Late Visean to Serpukhovian age of the foreland sedimentary basin in which they emplace ([Engel et al., 1980] and [Feist & Galtier, 1985]).

The Axial Zone consists of metamorphic rocks (micaschists, gneiss, and a small amount of marbles), migmatites, and post-migmatitic plutonic rocks globally arranged in a domal shape, which is well designed by the foliation attitude and the geometry of the micaschist-gneiss contact ([Gèze, 1949] and [Schuiling, 1960]). To the east, a tight synform of micaschists subdivides the Axial Zone dome into the Espinouze and Caroux sub-domes (Fig. 2). The northeastern limit of the Axial Zone is the Graissessac brittle dextral-normal fault that controls the opening of the Late Carboniferous (Gzhelian) Graissessac coal basin ([Bogdanoff et al., 1984] and [Echtler & Malavieille, 1990]). This brittle structure must not be confused with the Mont-de-Lacaune Fault (MLF) that separates migmatites and granites from high temperature-low pressure micaschist and marbles from south to north, respectively (Fig. 2). The MLF is a ductile structure characterized by a north dipping foliation and a mineral lineation inclined of nearly 45° to the east. Subsequently, the MLF acted as a normal fault with a dextral wrench component. East of Graissessac, Early Permian continental rocks, characterized by red sandstone and mudstone that form the Lodève basin, unconformably overlie the Late Carboniferous terrigeneous rocks. The southwestern termination of the axial zone, or Nore massif, is separated from the main part of the dome by the Eocene north-directed reverse fault of Mazamet (Fig. 2). This structure, related to the Pyrenean orogeny, does not alter significantly the Variscan architecture of the Montagne Noire Axial Zone. Although widely acknowledged, the dome structure of the Montagne Noire Axial Zone has been variously interpreted. A discussion of the tectonic setting of this structure is beyond the scope of this paper; the reader can refer to Soula et al. (2001). In spite of the controversy on the Montagne Noire dome emplacement, there is a large consensus on the relative chronology of the tectonic events, namely: 1) recumbent folding and thrusting, 2) crustal melting and doming, 3) post-migmatitic granitoid emplacement, and 4) infill of the Graissessac coal basin. However, the available absolute age constraints are restricted to orthogneiss protoliths and late granitoids ([Hamet & Allègre, 1976], [Ducrot et al., 1979], [Lévêque, 1990], [Matte et al., 1998], [Roger et al., 2004] and [Cocherie et al., 2005b]). Presently, the age of the migmatitic episode is not documented.

4. The Montagne Noire Axial Zone

Several rock types are recognized in the Montagne Noire Axial Zone. Augen orthogneiss yield zircon U–Pb ages of 471 ± 4 Ma, 456 ± 3 Ma and 450 ± 6 Ma interpreted as the emplacement age of the granites ([Roger et al., 2004] and [Cocherie et al., 2005a]). These Ordovician granitoids intruded a sedimentary sequence of grauwacke, pelite, quartzite, and rare marble with interlayered acidic or mafic magmatic beds ([Demange et al., 1996] and [Alabouvette et al., 2003]). Therefore, the Montagne Noire Axial Zone can no longer be considered as a Precambrian basement covered by a Paleozoic series (outdated interpretation on map by Demange et al., 1996). These rocks experienced a high temperature-low pressure metamorphism with a high temperature gradient of ca 50 °C/km and tight isogrades roughly parallel to the dome shape ([Bard & Rambeloson, 1973], [Demange et al., 1996], [Soula et al., 2001] and [Alabouvette et al., 2003]). This thermal structure agrees well with the progressive crustal melting observed in the centre of the dome. In the dome core, the migmatites progressively grade from metatexites, with leucosomes parallel to the protolith foliation, to diatexite where foliation is absent, and finally to the Laouzas cordierite anatectic granite containing host rocks preserved as metre to kilometre sized septa ([Gèze, 1949] and [Demange et al., 1996]; [Fig. 3] and [Fig. 4]). An earlier, presently undated, high-pressure metamorphism is documented by rare occurrences of kyanite in micaschist, and eclogite blocks in gneiss ([Demange, 1985] and [Alabouvette et al., 2003]).

The northwestern part of the Axial Zone is occupied by the Montalet pluton. This peraluminous granite is represented by two lithologies, a biotite-rich facies and a garnet-rich one (Fig. 5). The Montalet pluton is considered as an early body ([Demange et al., 1996] and [Alabouvette et al., 2003]). However, as documented in the following section, the magmatic zircon and monazite in this granite yield radiometric ages similar to those obtained for the Laouzas anactectic granite and the migmatites. Several, small sized, late to post-migmatitic plutons intrude the Axial Zone migmatites (Fig. 2). They are either biotite-rich granite (e.g. Anglès granite) or muscovite–biotite ± garnet leucogranites (e.g. Soulié, Vialais granites). Lastly, several generations of garnet–tourmaline pegmatite and aplite dykes and sills intrude the above-described metamorphic and plutonic rocks (Collot, 1980).

5. Analytical procedures

5.1. EPMA dating

Three starting assumptions are required to determine U–Th–Pb_{tot} age by using EPMA: 1) common Pb is negligible as compared to the amount of thorogenic and uranogenic lead (Parrish, 1990); 2) no radiogenic Pb loss has occurred since system closure, Pb content is not significantly affected by diffusion (e. g. [Cocherie et al., 1998], [Crowley & Ghent, 1999] and [Zhu & O'Nions, 1999]); 3) a single age is involved at the size level of each individual spot analysis. After comparison with conventional isotopic U–Pb age determinations, it is now accepted that EPMA resolution allows inclusions and altered domains that could potentially contain common Pb to be avoided.

The monazite grains were studied either after extracted by crushing before being mounted in resin or directly by the mean of petrographic thin sections. Both procedures allow the monazite grains to be analyzed using a Cameca SX 50 electron microprobe (cooperated by BRGM and Orléans University, France). Systematic BSE study was performed to investigate monazite micro-texture for all analyzed grains. Obviously, the *in situ* analysis of monazite grains directly in thin sections is more convenient to study age in relation to its petrographic context. This is possible if monazite grains are visible in the thin section and if they are large enough to be sure to avoid border effect when using EPMA.

The analytical procedure for monazite was detailed in (Cocherie et al., 1998) and (Cocherie et al., 2005b); see also Cocherie and Robert, 2008). The interference of YLγ on PbMα is subtracted offline by applying a coefficient of interference to the value of Y. The different interference corrections have been validated by dating several monazite samples using this method and using conventional isotopic methods (Cocherie et al., 1998). An accelerating voltage of 20 kV, and a beam current of 100 nA were applied. According to this procedure, the calculated detection limit (2σ) is 150 ppm for Pb, U and for Th, whereupon an absolute error of 150 ppm is also taken. A systematic relative error of 2% is considered for Th (whose concentration is generally above 7500 ppm), and also for U concentrations above 7500 ppm in order to avoid an unrealistic low error for U-enriched grains (Cocherie and Legendre, 2007). For monazite the standards were galena (PbS) for Pb, uraninite (UO_2) for U, thorianite (ThO_2) for Th, endmember synthetic phosphates (XPO_4) for each rare-earth element (REE) and Y, apatite for P and andradite for Si and Ca.

If two or more homogeneous age domains are separated by a gap lower than the analytical error on each individual spot analysis age, these can be identified by suitable isochron diagrams ([Suzuki & Adachi, 1991], [Cocherie et al., 1998], [Cocherie & Albarède, 2001] and [Suzuki & Kato, 2008]). It has been shown how to provide precise ages ± 5 to 10 Ma (2σ)

using the most suitable isochron diagram according to the geochemistry of the studied grains (Cocherie et al., 2005b).

A Microsoft Excel add-in program, called *EPMA dating*, was created for determining U–Th–$Pb_{tot.}$ ages from electron probe microanalyzer (EPMA) measurements (Pommier et al., 2002). All the parameters needed to calculate mean and intercept ages are computed ready to be plotted using the *ISOPLOT* program (Ludwig, 2003) in order to obtain statistics from suitable diagrams. Finally, *EPMA dating* produces (1) the U–Th–Pb age at the centroid of the best fit line, and (2) the Th–Pb age (intercept with Th/Pb axis) and the U–Pb age (intercept with U/Pb axis) from the Th/Pb vs. U/Pb diagram. All the calculations were done at 2σ level. A special care was taken on the MSWD (Mean Squared Weighted Deviation) which must be below $1+2/(2/f)^{0.5}$ (f : degree of freedom = number of analyses − number of dated events) in order to validate age calculation (Wendt and Carl, 1991) for a single age population. Using such a diagram, a single population must also lead to a regression line showing the same slope as the corresponding theoretical isochron. In other words, the U–Pb and Th–Pb age intercepts must be similar within the uncertainties on these ages.

5.2. SIMS dating

Zircons were dated using the SIMS (IMS 1270) at CNRS, CRPG Nancy (France), according to the procedure described by (Deloule et al., 2001) and (Deloule et al., 2002) The areas analyzed (~ 25 µm) were selected after studying images of the grains obtained by cathodoluminescence and by transmitted light microphotography. The geostandard 91500 zircon from Ontario (Canada), dated at 1065 Ma (Wiedenbeck et al., 1995) is used for $^{238}U/^{206}Pb$ calibration. In general, areas very rich in U (> 2000–3000 ppm) were not selected in order to avoid, firstly, moving away from the area of validity of the U–Pb calibration line and, secondly, the risk of losses of radiogenic Pb, in relation to the metamictisation. For the relatively recent zircons (< 1000 Ma), the imprecision of the $^{206}Pb/^{204}Pb$ ratio becomes critical; one then uses the Concordia diagram (Tera and Wasserburg, 1972), modified by Compston et al. (1992), in which one plots the $^{207}Pb/^{206}Pb$ and $^{238}U/^{206}Pb$ ratios, not corrected for common Pb. In the absence of common Pb, the analyses of areas not affected by recent Pb* loss after the crystallisation of the zircon or by inherited cores are spread along this Concordia (Williams, 1998). Although the variable quantities of common Pb adversely affect the values of the two ratios, these kinds of points form a straight line passing through the composition of common Pb ($^{207}Pb/^{206}Pb$) at the estimated age of the system given, in a first approximation, by the average $^{238}U/^{206}Pb$ ages stemming from the concordant analyses. The extrapolation of this line on the Concordia defined the sought age. This is what is called a correction of common Pb by the ^{207}Pb method and not by the ^{204}Pb method, as in the case of the conventional diagram. Using this correction method, one calculates the $^{206}Pb^{*}/^{238}U$ (Pb* = radiogenic Pb) ratios for each point. Whatever the used analytical approach, all the calculations were made at 2σ (95% confidence limit) using the *ISOPLOT* program (version 3) of Ludwig (2003). On the other hand, in the case of the data obtained using the SIMS, the uncertainties are given at 1σ in the corresponding table and, in the same way, the error ellipses are given at 1σ in order to make the figures easier to read.

6. Geochronological results

New geochronological data are reported on coexisting monazite and zircon, for migmatites, anatectic granitoids and late-migmatitic plutons from the Axial Zone of the Montagne Noire. Monazite and zircon crystals were selected from a mineral separate, after crushing the samples, mounted in epoxy mount, and polished to approximately half thickness. For five of the samples, monazite was analyzed in thin section in its petrographic context. Monazites were imaged with a backscattered electron detector (BSE) in a scanning electron microscope (SEM) before collecting U–Th–Pb_{tot} data with an EPMA. Zircons were imaged with a cathode-luminescence detector (CL) in a SEM before U–Pb isotopic analysis by SIMS.

6.1. Migmatites

6.1.1. La Salvetat migmatite

6.1.1.1. U–Th–Pb_{tot} monazite dating

This rock is a diatexite (Fig. 4) sampled near the La Salvetat village (GPS location: N43.61754, E 2.75685). Five monazite grains were analyzed on two thin sections. The grains, with sizes ranging from 50 to 150 µm, are included in biotite (Fig. 6a, b). Their shapes are subhedral or rounded, and rarely cracked. The back-scattered electron (BSE) scan electron microsope (SEM) images of the analyzed grains show a well developed patchy zoning structure but no regular growth zoning (Fig. 6c).

The BSE images are representative of the electronic density, thus Th- and U-enriched domains appear clearer than other domains; note that generally the weight percentage of Y is too low to provide significant change in BSE images. Th- and U-enriched domains can show similar Th/U ratio as those observed in Th- and U-depleted domains, leading to contrasting BSE images associated to constant Th/U ratio. Thus, rather constant Th/U ratio (Fig. 7; Table 1) is observed for La Salvetat monazite despite BSE images show contrasting domains. This constant Th/U ratio results in a large error envelop around the regression line. Despite the lack of a large spread of the representative spot analyses, the slope of the regression line is very close to the theoretical isochron. This demonstrates that all the spot analyses are similar in age within the analytical uncertainties. A mean age of 327 ± 7 Ma was calculated at the centroid of the population. The MSWD (1.5) is only slightly above the upper limit when a population of 48 analyses is taken into account (1.4, see Wendt and Carl, 1991), because none of the data were rejected. Therefore the analyzed grains will be considered as a single population. A detailed examination of the data and Th/Pb vs. U/Pb plot makes visible three groups of composition according to the Th/U ratio. However, this diagram demonstrates that they cannot be distinguished in age (within the analytical resolution of EPMA dating) because the regression line has the same slope as the theoretical isochron at 327 Ma**.** This age is interpreted as the crystallization age of the monazite. No inherited domain was detected.

6.1.1.2. U–Pb zircon dating

This sample contains abundant oscillatory zoned elongate zircon crystals. Most of the 34 SIMS analyses performed in 26 crystals plot along or near the Concordia curve, and define a cluster at around 550 Ma. One discordant analysis yield a $^{207}Pb^*/^{206}Pb^*$ age of 2365 Ma. Special attention has been paid to analyze the youngest possible domains of the zircons, including the pyramidal extremities of the crystals. In spite of this effort, only three analyses seem to date the Variscan migmatization. These three analyses project on the Concordia curve at an age of 306 ± 6 Ma (^{207}Pb corrected $^{206}Pb/^{238}U$ age).

One out of three is significantly discordant due to common Pb contribution (not corrected in this diagram), but it can be considered in the calculation assuming a mixing line with the common Pb composition in the Variscan times. The calculated age is 306 ± 6 Ma. The cluster of analyses around 550 Ma can be interpreted in two ways. (1) A single age was recorded and various degree of radiogenic Pb* loss results in a shift of more than 50% of the analyses. (2) Two main inherited protoliths were recorded at 562 ± 6 Ma (MSWD = 0.8, n = 11) and 530 ± 5 Ma (MSWD = 1.4, n = 13). A third one could also be dated at 478 ± 13 Ma. We think that an extended recent Pb* loss should provide a wider range of variation of the data along the $^{238}U/^{206}Pb$ axis. Therefore, in addition to the 562 Ma age, 530 and 478 Ma could also be significant on a geological point of view (see discussion section, below).

It must be underlined that only three spot analyses are considered for the age calculation at 306 Ma. In addition, only two of them are concordant at 304 ± 8 and 315 ± 16 Ma (2σ) while monazite was dated at 327 ± 7 Ma (2σ). Thus, within the analytical uncertainties and considering only these two spot analyses on zircon overgrowths we cannot really conclude that monazite grains crystallized significantly before or at the time of zircon recrystallization. The usual conception is that zircon ages tend to be older than monazite ages within the same rock. Furthermore, recent experimental data (Kelsey et al., 2008) led to the same conclusion. However, we also studied numerous monazite and zircon samples from natural migmatites. It was demonstrated that monazite can remain as a residual accessory phase while inherited zircon grains were dated at the same age but also show overgrowth during the migmatitic stage, 80 Ma later, not visible on monazite grains (Cocherie et al., 2005b). Several unpublished data from leucocratic granites show the same trend. It seems to demonstrate first that monazite is a very robust mineral up to the temperature of zircon overgrowth and second that there is a lack of some chemical elements required for the overgrowth of preexisting monazite during migmatization.

6.1.2. Ourtigas migmatite

6.1.2.1. U–Th–Pb$_{tot}$ monazite dating

Two samples (Ourt1 and Ourt2) of the metatexite developed at the expense of an augen orthogneiss, the foliation of which remains well preserved (Fig. 3), were collected at the Ourtigas pass (GPS location: N43.63657, E2.97628). The monazite grains are quite similar to those from the Salvetat migmatites (Fig. 8). Seven and three monazite grains from Ourt1 and Ourt2, respectively were separated and mounted in polished sections. Two age populations associated with different monazite grains can be identified from the Ourt1 sample. The first population consists of 29 analyses obtained on three grains, which define a consistent regression line in the Th–Pb vs. U–Pb diagram (Fig. 9). The intercept ages are rather well defined (U–Pb age: 314 + 14–16 Ma and Th–Pb age: 347 + 26–22 Ma) and similar within the errors. A mean age of 326 ± 4 Ma (MSWD = 0.71) was calculated at the centroid of the population. Four grains define the second population that provide a distinct regression line when plotting 30 analyses in the Th–Pb vs. U–Pb diagram (Fig. 9). The intercept ages are similar within the errors on these ages: U–Pb age: 420 + 48–51 Ma and Th–Pb age: 468 + 17–15 Ma. A mean age of 458 ± 9 Ma (MSWD = 0.62) was calculated at the centroid of the population. No textural feature allows us to distinguish the two monazite populations yielding 326 Ma and 458 Ma ages. In addition, it is surprising that no overgrowths were observed on the cores of old monazite grains. Such overgrowths were observed for instance on monazite grains from French Massif central in Puylaurent migmatite (Bé Mézème et al., 2006) or in St Laurent granite (Cocherie et al., 2005b). We suggest that the older grains were not in equilibrium with the magma from which the younger grains crystallized. They can be inherited from the wall rocks during the emplacement the migmatitic melt during Variscan times.

Fifty-four analyses were recorded from three monazite grains from Ourt2 sample (Fig. 7). The Th/U ratio changes significantly, leading to a well-defined slope of the regression line. This slope is very similar to that of the theoretical isochron. A mean age of 524 ± 7 Ma (MSWD = 1.3) was calculated at the centroid of the population.

6.2. Anatectic granitoids

6.2.1. Laouzas cordierite granite

6.2.1.1. U–Th–Pb$_{tot}$ monazite dating

The Laouzas cordierite granite represents one end-member of the progressive evolution from partially melted country gneiss to anatectic granite through metatexite and diatextite. The dated sample (GPS location: N43.63363 E2.75685) contains numerous enclaves of the metamorphic country rocks (Fig. 4). Alike for the migmatite, in the Laouzas granite, the monazite occurs as inclusion in biotite. Euhedral monazite grains with size ranging from 50 to 150 μm, commonly exhibit a patchy zoning, and more rarely contain thorite inclusions. The monazite grains of the Laouzas cordierite granite were directly investigated on thin section. Fifty-four spot analyses were performed on five grains by using the EPMA technique. Due to rather constant Th/U ratio, the spot analyses are clustered in the Th/Pb vs. U/Pb diagram (Fig. 10) leading to large errors on the intercept ages (U–Pb age: 321 + 65–74 Ma and Th–Pb age: 336 + 23–20 Ma). However, it is noteworthy that the slope of the regression line is very close to that of the theoretical isochron. A mean age of 333 ± 6 Ma (MSWD = 0.65) was calculated at the centroid of the population (n = 54).

6.2.1.2. U–Pb zircon dating

Zircons from this sample are elongate and oscillatory zoned (Fig. 11b). Thirty-two SIMS analyses were performed on 27 crystals (Table 2c; Fig. 12b). Most of the analyses plot around 550–520 Ma. In spite of efforts to retrieve a Variscan intrusion age, only two analyses can be related to crystallization of the granite itself. The age of 299 ± 8 Ma derived from theses two analyses is probably affected by Pb* loss and is not regarded as a reliable estimate. Taking into account the uncertainties on the oldest spot analyses, more than one age must be considered. Again, we favour the hypothesis considering that two main inherited protoliths were recorded at 552 ± 5 Ma (MSWD = 1.4, n = 18) and 520 ± 7 Ma (MSWD = 2.0, n = 12). However, similarly to La Salvetat zircons, because the second group of analyses is not concordant, we must consider the hypothesis that some radiogenic Pb* loss happened, making the age of 520 Ma not significant. Nevertheless, as for La Salvetat inherited zircons, a recent Pb* loss should provide a much wider range of variation of the data along the $^{238}U/^{206}Pb$ axis. Therefore, the 552 Ma and 520 Ma ages can be both significant from a geological point of view.

6.2.2. Montalet granite

Three samples of the Montalet granite have been analyzed. Two of them belong to the biotite-rich facies and one to the garnet-rich facies (Fig. 5). In all three samples, monazite occurs as inclusion in biotite or more rarely as an interstitial phase along biotite and K-feldspar grain boundaries. The monazite grains of the garnet-rich and biotite-rich facies are anhedral and without zoning (Fig. 13) which does not mean necessarily that they are not chemically zoned. Indeed, the large scatter of points in the Th/Pb vs. U/Pb diagram for one the Montalet biotite-rich facies and the garnet-rich facies suggest that the monazite is chemically zoned. They have been studied directly on thin sections. Furthermore, the garnet-rich facies has also been dated on separated zircon by SIMS.

6.2.2.1. Garnet rich-facies

This sample (GPS location: N43.61897, E2.60599) is an oligoclase, K-feldspar, fine-grained leucocratic monzonite with millimetre-sized almandine (Fig. 5). Fifty-eight spot analyses were performed on five grains by using the EPMA technique. Due to a rather small amount of Th and U, the ellipse errors associated to each individual analysis are large (Fig. 10). The theoretical isochron remains within the uncertainty defined by the error envelop of the regression line. A mean age of 327 ± 7 Ma (MSWD = 0.95) was calculated at the centroid of the population.

The zircon grains from the same sample (garnet rich facies) were also investigated (Fig. 12c; Table 2b). Analyzed grains are generally elongated (100 to 150 µm) needles but they exhibit contrasting internal structure. The cathodoluminescence images of representative grains are shown on Fig. 11c. Some euhedral or subhedral grains exhibit a core and rim structure.

Twenty-five spots were performed on 21 zircon grains. A significant number of analyses show common-Pb contribution in the uncorrected Tera and Wasserburg diagram (Fig. 12c). However, a nice mixing trend between common Pb and radiogenic Pb provide an intercept age at 324 ± 3 Ma (MSWD = 1.4) using 9 analyses. This age is similar to the age calculated from the monazite of the same granite. Abundant inherited crystals yield dates at around 460 Ma, 1000 Ma and even 2700 Ma (Table 3).

6.2.2.2. Biotite-rich facies

The dated sample (GPS location: N43.62194, E2.50402) is an oligoclase, biotite-rich medium-grained monzogranite with abundant K-feldspar megacrysts ([Fig. 5] and [Fig. 13]). Monazite has been investigated directly on thin section. The grains are rather small (around 40–70 µm). Some of them show a patchy zoning but no inherited cores, sixteen grains have been analyzed. The U/Pb and Th/Pb intercept ages are similar within errors: 333 + 67/− 55 Ma and, 326 + 6.9/− 6.6 Ma respectively (Fig. 10). In addition, the MSWD of 1.1 indicates that the population of 159 analyses is statistically homogeneous within the analytical errors (Wendt and Carl, 1991). Thus, the monazite grains lead to a mean age of 333 ± 4 Ma (at 95% confidence level) calculated at the centroid.

The second sample is also a medium-grained mesocratic porphyritic granodiorite petrologically similar to the previous one (GPS location: N43.64770, E 2.59933). The chemical composition of the monazite grains was very favourable for U–Th–$Pb_{tot.}$ geochronology since they exhibit a high U and Th content, and a wide range of variation for the U/Th ratio. Consequently, the ellipses errors are small and the data plot favourably in the Th/Pb vs. U/Pb diagram (Fig. 10) showing a narrow error envelop. The intercept ages are very well defined (U–Pb age: 482 + 21–23 Ma and Th–Pb age: 507 + 13–12 Ma) and similar within the errors. A mean age of 499 ± 6 Ma (MSWD = 1.1) was calculated at the centroid of the population (n = 96).

6.3. Late to post migmatitic granites

Among the numerous kilometre-sized plutons that intrude into the migmatites, the Anglès, Vialais, and Soulié massifs have been dated by monazite U–Th–Pb monazite method.

6.3.1. Anglès pluton

The analyzed sample (GPS location: N 43.56441, E2.55789) is a medium grained monzonite in which biotite exhibits a clear planar preferred orientation. Three separated monazite grains were mounted in polished section. The SEM back-scattered electron images show subeuhedral, cracked grains without chemical zoning (Fig. 13c and d). A well-defined regression line that perfectly fits with the theoretical isochron was obtained after plotting 56 analyses in the Th–Pb vs. U–Pb diagram (Fig. 15a). The intercept ages are rather well defined (U–Pb age: 322 + 34–40 Ma and Th–Pb age: 327 + 31–26 Ma) and they are identical within the errors. In other words the regression line and the theoretical isochron are almost identical. A mean age of 325 ± 7 Ma (MSWD = 1.2) was calculated at the centroid of the population.

6.3.2. Vialais pluton

This medium-grained leucogranite (GPS location: N 43.64436 E 2.96685) contains rare garnet grains and does not exhibit a mineral preferred orientation. Five separated monazite grains were mounted in polished section. Th and U contents are high and the Th/U ratio show a wide range of variation that makes the Th–Pb vs. U–Pb representation very precise (Fig. 15b). The regression line and the theoretical isochron are very close. A mean age of 320 ± 3 Ma (MSWD = 0.92) was calculated at the centroid of the population.

6.3.3. Soulié pluton

The analyzed sample (GPS location N43.53352 E2.66002) is a two-micas monzogranite with globular quartz and large muscovite grains. The SEM BSE images reveal subeuhedral , slightly fractured monazite grains without chemical zoning (Fig. 13c). Three separated monazite grains were mounted in polished sections. A well-defined regression line was obtained after plotting 68 analyses in the Th–Pb vs. U–Pb diagram (Fig. 15). The intercept ages are rather well defined (U–Pb age: 298 + 22–23 Ma and Th–Pb age: 325 + 9–8 Ma) and they are identical within the errors. The regression line and the theoretical isochron are almost identical. A mean age of 318 ± 4 Ma (MSWD = 1.08) was calculated at the centroid of the population.

7. Discussion

7.1. Geological significance of the new results

The U–Th–Pb_{tot} monazite ages presented above are consistent and geologically meaningful. The ages of the La Salvetat, and Ourtigas migmatites around 327–326 Ma are in agreement with that of the Laouzas anatectic granite at 333 ± 6 Ma. These late Visean ages are also similar to the emplacement age of the Montalet pluton dated on monazite at 327 ± 7 Ma and on zircon at 324 ± 3 Ma. Therefore, data available today do not support the assumption that the Montalet granite is an early pluton ([Demange et al., 1996] and [Alabouvette et al., 2003]). Furthermore, the coeval character of the migmatites and anatectic granitoids is consistent with petrofabric and AMS analyzes showing that the Montalet granite, Laouzas granite, and migmatites experienced the same sub-solidus to post-solidus deformation stages during the doming of the Montagne Noire Axial Zone (Charles et al., 2009). The new results demonstrate the abundance of Neoproterozoic, Cambrian and Ordovician ages inherited zircon and monazite grains. Such "old" ages are already identified in the Montagne Noire, for instance in the Héric, Plaisance, Mazamet and Mendic orthogneiss (Fig. 16, [Hamet & Allègre, 1976], [Ducrot et al., 1979], [Roger et al., 2004] and [Cocherie et al., 2005a]). The ca. 560–530 Ma ages are interpreted as the crystallization ages of the granite protolith of the migmatites and anatectic granites. Furthermore, the Early Ordovician ages (ca 480 Ma) also correspond to the alkaline granites related to the rifting of Armorica from Gondwana, and transformed into orthogneiss during the eo-Variscan D0 and D1 events. Moreover, Paleoproterozoic and Archean zircons, recovered from the migmatites and anatectic granitoids, represent unmelted relict grains inherited from the source of the Early Paleozoic magmatic rocks. Archean or Paleoproterozoic ages are now well identified in many Variscan French massifs, such as the Pyrénées or Massif Central ([Deloule et al., 2002], [Cocherie et al., 2005a], [Melleton et al., 2010a] and [Melleton et al., 2010b]).

Our ages of the late migmatitic granites range from 325 ± 7 Ma to 318 ± 4 Ma. These dates are also in agreement with field and petrofabric observations showing that these plutons emplaced within an already foliated migmatite. The monazite age at 325 ± 7 Ma of the Anglès biotite massif is close to the ages of the migmatite and contemporaneous anatectic granites. In addition to field observations showing numerous biotite enclaves, host rock xenoliths and poorly defined boundaries, this date is in agreement with a late-migmatitic setting for the Anglès pluton.

The Soulié biotite–muscovite granite does not present a macroscopic mineral preferred orientation. Its chemistry and young age at 318 Ma suggest that this massif belongs to the most differentiated magmas such as the late pegmatite dykes that emplaced during the late magmatic stages in the Axial Zone of the Montagne Noire.

Lastly, the 320 ± 3 Ma monazite age presented in this paper for the Vialais pluton is slightly younger than the zircon U–Pb TIMS age at 327 ± 5 Ma obtained previously for the same massif (Matte et al., 1998). However, these two ages are identical within the analytical uncertainties. As presented above, available maps and field investigations clearly show that the Vialais pluton intrudes at high angle into the foliated migmatites (Bogdanoff et al., 1984).

7.2. Late Visean partial melting in the French Variscan belt

The Montagne Noire Axial Zone represents the largest area of the Visean migmatites in the French Massif Central. In the recent years, several migmatite occurrences have been radiometrically dated of Late Visean in several parts of the French Massif Central (Fig. 1). In northern Cévennes, the migmatites that crop out along the southern edge of the Late Carboniferous Velay dome have often not been distinguished from the ca 300 Ma Velay migmatites (Ledru et al., 2001). However, several lines of evidence argue for an earlier crustal melting event (Montel et al., 1992). The monazites from the northern Cévennes migmatites yield U–Th–Pb ages at ca 330–325 Ma, and they are intruded by two-micas granites dated at 320–315 Ma ([Cocherie et al., 2005b] and [Bé Mézème et al., 2006]). To the west, migmatites that crop out in the southern part of the Millevaches massif have been dated between 337 and 328 Ma by the U–Th–Pb method on monazite (Faure et al., 2009b). Lastly, in the northeastern French Massif Central, the Autun migmatites (Fig. 1) yield monazite chemical ages at ca 330 Ma (Choulet, personal communication). Zircon from migmatites found in the central part of the Vosges yields U–Pb ages at ca 340 Ma (Schaltegger et al., 1999; Fig. 17).

More to the South, the Variscan Pyrenees presents great similarities with the Montagne Noire area. There, migmatitic domes and anatectic granitoids are recognized for a long time in the Hospitalet, Aston and Canigou massifs but smaller outcrops are also identified (e. g. [Zwart, 1986], [Soula et al., 1986], [Vissers, 1992], [Carreras & Capella, 1994], [Mezger, 2005] and [Denèle et al., 2007]; Fig. 17). Although the age of the migmatite is not available yet, the upper limit for crustal melting is provided by the Late Carboniferous age of the granitoids intruding the migmatite (Soula et al., 1986).

In the southern part of the Massif Armoricain, which also belongs to the northern Gondwana domain, migmatites are well exposed in the Vendée and Morbihan areas (Fig. 17; [Cogné, 1960], [Audren, 1990], [Goujou, 1992] and [Brown, 2005]). The Morbihan migmatites have recently been dated at ca 330–325 Ma by EPMA method on monazite (Turrillot et al., 2009). Furthermore, the migmatites that form the main part of the Léon domain in the northwest Armorican Massif yield also 335–327 Ma monazite chemical ages (Faure et al., 2010).

East of the Cévennes fault, Variscan migmatites are also well exposed in the external crystalline massifs of the Western Alps, and in the Maures, and Corsica–Sardinia Massifs ([Guillot & Ménot, 2009], [Corsini & Rolland, 2009] and [Rossi et al., 2009]; Fig. 17). In all of these areas, radiometric constraints on the migmatization are still rare. Recently, monazite chemical dating of the migmatites that crop out in the Maures Massif indicates a Late Visean–Serpukhovian age (Melleton et al., in review).

In addition to the migmatitic domains, the Late Visean partial melting is well represented in the Variscan French massifs. Volcanic and volcano-sedimentary rocks of the "Tufs anthracifères" series crop out widely in the northern part of the French Massif Central and Vosges ([Fig. 1] and [Fig. 17]). Similar rocks are also developed in the Châteaulin and Laval basins in the North-Central Armorican domain (Fig. 17). Therefore, at the scale of the entire French Variscan belt, the Late Visean crustal melting corresponds to an important episode responsible for the emplacement of huge volumes of melts. Fig. 17 shows that the distribution of the areas that experienced the Late Visean crustal melting are widely scattered.

In most of areas, the tectonic setting of the Late Visean migmatites is poorly constrained or remains controversial. Dome structures are documented in a few places such as the Montagne Noire, the Pyrénées or in Vendee. Several tectonic interpretations, namely compressional, extensional, trans-tensional or diapiric settings have been proposed, a discussion of these models is beyond the scope of this paper (cf. [Van Den Driessche & Brun, 1992] and [Soula et al., 2001] for extensive reviews).

7.3. A mantle origin for the heat?

The Late Visean partial melting can be situated in a larger perspective at the scale of the French Variscan segment. Lava flows, and migmatitic–plutonic complexes represent the shallow and deep records of the same crustal melting event. Tectonically, melting developed during the North-directed and South-directed thrusts observed in the Ardenne and Montagne Noire–Pyrénées domains, respectively, whereas, in the northern part of the French Massif Central, the Late Visean Tufs anthracifères magmatism is coeval with the onset of the NW–SE post-collisional extension e.g. Faure et al., 2005). The Late Visean crustal melting occurred after the main phase of continental collision between three continental masses, namely from North to South, Laurussia, Mid-German Crystalline Rise-Léon, and Gondwana. The Rheic-North Phyllite Zone suture and Le Conquet–Penzé–Tepla suture separate these continents ([Fig. 16] and [Fig. 17]). As a whole, the Carboniferous tectonic evolution is controlled by a south-directed subduction (e.g. [Matte, 1991], [Matte, 2001], [Franke, 2000], [Faure et al., 2002], [Faure et al., 2009a] and [Faure et al., 2009b]). In this framework, the migmatitic, plutonic and volcanic complexes presented above are located in the upper plate, i.e. in the units derived from Gondwana, of the convergent system. Thus, as sometimes emphasized, the Carboniferous Variscan geodynamic setting can be compared to an Andean orogen (e. g. Schulman et al., 2009).

The question of the heat source able to produce such a continental-scale melting arises. A first explanation would link the heat release with the un-thickening phase that generally follows continental collision. However, another possibility is to consider a mantle heat contribution. This explanation requires the thinning of the subcontinental mantle lithosphere and its replacement by a hot asthenospheric mantle that might be achieved by various mechanisms such as delamination, magmatic underplating or convective ablation.

Great attention has been paid to the Andean Belt as a typical example of an orogen developed in the upper plate of a converging system. Numerous works emphasized the importance of partial melting in the thick crust of the Andes Cordillera (e.g. [ANCORP Working Group, 2003], [Schilling et al., 2006] and [Oncken et al., 2006] and enclosed references). Interestingly, numerical modelling showed that heat necessary to produce molten layers in the crust must be provided by the asthenosphere mantle, and that convection of partially molten crust must have played an important role to account for the present magmatism of the Central Andes (Babeyko et al., 2002). Tentatively, we speculate here that a similar mechanism might be responsible for the development of the widespread crustal melting in the Variscan belt. After the main continental amalgamation was completed in Early Carboniferous, the lithosphere mantle was thinned and heat transfer from the asthenosphere triggered the melting of the middle crust giving rise to intracustal convection and development of anatectic granite–migmatitic complexes throughout the entire belt (Fig. 18).

8. Conclusion

This EMPA and SIMS geochronological study on monazite and zircon, respectively allows us to clarify the age of the partial melting in the Montagne Noire Axial Zone. The Visean (ca 333–326 Ma) age of the migmatites and anatectic granitoids is in good agreement with the ages recovered in other massifs of the FrenchVariscan Belt. An Andean-type orogeny, in which the migmatitic regions belong to the upper plate appears as a possible model to account for the geodynamic setting of this Carboniferous crustal melting event. However, the mechanisms of mantle thinning remain a matter of debate. Furthermore, zircon yields SIMS Archean, Paleoproterozoic, Neoproterozoic–Cambrian and Ordovician ages. These grains are interpreted as inherited from the protolith souces of the melts. They suggest that the Axial Zone of the Montagne Noire contains numerous Precambrian and Early Paleozoic plutonic rocks. The tectonic setting of these protoliths remains to be clarified.

Acknowledgements

C. Gilles (BRGM) and O. Rouer (ISTO) are acknowledged for their technical assistance in operating EPMA. The authors also acknowledge M. Champenois, E. Deloule, and D. Mangin (CRPG-CNRS-Nancy) in operating the IMS 1270. E. Bé Mézème thanks the Conseil Régional du Centre for providing a scholarship during his Ph.D. Field expenses and laboratory analyses have been funded by the Programme de la Carte Géologique de France, managed in BRGM. B. Bingen and an anonymous reviewer are thanked for constructive comments to improve the initial version.

References

Alabouvette et al., 2003 Alabouvette, B., Demange, M., Guérangé-Lozes, J., Ambert, P., 2003. Notice explicative de la carte géologique au 1 :250000 de Montpellier, Bureau de Recherches Géologiques et Minières, Orléans, France.

ANCORP Working Group, 2003 ANCORP Working Group, Seismic imaging of a convergent continental margin and plateau in the Central Andes (Andean Continental Research Project 1996, ANCORP'96), *Journal of Geophysical Research* **108** (B7) (2003), pp. 1–25.

Arthaud, 1970 Arthaud, F., 1970. Etude tectonique et microtectonique comparée de deux domaines hercyniens : les nappes de la Montagne Noire (France) et l'anticlinorium de l'Iglesiente (Sardaigne). Ph.D. thesis, Université de Montpellier.

Arthaud & Matte, 1977 F. Arthaud and P. Matte, Synthèse provisoire sur l'évolution tectonique et les raccords entre les segments hercyniens situés autour du bassin nord-Baléare (sud de la France, Espagne, bloc corso-sarde), *La chaîne varisque d'Europe moyenne et occidentale, coll. intern* **243**, CNRS (1977), pp. 497–513.

Audren, 1990 C. Audren, Evolution tectonique et métamorphique de la chaîne varisque en Bretagne méridionale, *Schweitzerische Mineralogische und Petrographische Mittelunge* **70** (1990), pp. 17–34.

Babeyko et al., 2002 Y. Babeyko, S.V. Sobolev, R.B. Trumbull, O. Oncken and L.L. Lavier, Numerical models of crustal scale convection and partial melting beneath the Altiplano–Puna plateau, *Earth and Planetary Science Letters* **199** (2002), pp. 373–388.

Bard & Rambeloson, 1973 J.-P. Bard and R. Rambeloson, Métamorphisme plurifacial et sens de variation du degré géothermique durant la tectogenèse polyphasée hercynienne dans la partie orientale de la zone axiale de la Montagne Noire (massif du Caroux, sud du Massif Central français), *Bulletin de la Société Géologique de France* **15** (1973), pp. 579–586.

Bé Mézème et al., 2006 E. Bé Mézème, A. Cocherie, M. Faure, O. Legendre and P. Rossi, Electron microprobe monazite geochronology: a tool for evaluating magmatic age domains, *Examples from the Variscan French Massif Central. Lithos* **87** (2006), pp. 276–288.

Bellot, 2001 Bellot, J.-P., 2001. La structure de la croûte varisque du Sud-Limousin (Massif Central Français) et ses relations avec les minéralisations aurifères tardi-orogéniques: apport des données géologiques, gîtologiques, géophysiques et de la modélisation 3D. Ph. D. Thesis, Montpellier University, France.

Bogdanoff et al., 1984 Bogdanoff, S., Donnot, M., Ellenberger, F., 1984. Carte géologique de Bédarieux. Carte géologique de la France au 1:50000, n° 988, Bureau de Recherches Géologiques et Minières, Orléans, France.

Brown, 2005 M. Brown, Synergistic effects of melting and deformation: an example from the Variscan belt, western France. In: D. Gapais, J.P. Brun and P. Cobbold, Editors, *Deformation mechanisms, rheology and tectonics: from minerals to the lithosphere*, *Geological Society, London, Special Publication* **243** (2005), pp. 205–226.

Carreras & Capella, 199 J. Carreras and I. Capella, Tectonic levels in the Palaeozoic basement of the Pyrenees: a review and new interpretation, *Journal of Structural Geology* **16** (1994), pp. 1509–1524.

Charles et al., 2009 N. Charles, M. Faure and Y. Chen, The Montagne Noire migmatitic dome emplacement (French Massif Central): new insights from petro-fabric and AMS studies, *Journal of Structural Geology* **31** (2009), pp. 1423–1440.

Cocherie & Albarède, 2001 A. Cocherie and F. Albarède, An improved U–Th–Pb age calculation for electron microprobe dating of monazite, *Geochimica Cosmochimica Acta* **65** (2001), pp. 4509–4522.

Cocherie & Legendre, 2007 A. Cocherie and O. Legendre, Potential minerals for determining U–Th–Pb chemical age using electron microprobe, *Lithos* **93** (2007), pp. 288–309

Cocherie & Robert, 2008 A. Cocherie and M. Robert, Laser ablation coupled with ICP-MS applied to U–Pb zircon geochronology: a review of recent advances, *Gondwana Research* **14** (2008), pp. 597–608.

Cocherie et al., 1998 A. Cocherie, O. Legendre, J.J. Peucat and A.N. Kouamelan, Geochronology of polygenetic monazites constained by in situ electron microprobe Th–U–total Pb determination: implications for lead behaviour in monazite, *Geochimica Cosmochimica Acta* **62** (1998), pp. 2475–2497.

Cocherie et al., 2005a A. Cocherie, T. Baudin, A. Autran, C. Guerrot, M. Fanning and B. Laumonier, U–Pb zircon (ID-TIMS and SHRIMP) evidence for the early Ordovician intrusion of metagranites in the late Proterozoic Canaveilles Group of the Pyrenees and the Montagne Noire (France), *Bulletin de la Société Géologique de France* **176** (2005), pp. 269–282.

Cocherie et al., 2005b A. Cocherie, Mézème E. Bé, O. Legendre, M. Fanning, M. Faure and P. Rossi, Electron microprobe dating as a tool for understanding closure of U–Th–Pb system in monazite from migmatite, *American Mineralogist* **90** (2005), pp. 607–618.

Cogné, 1960 J. Cogné, Schistes cristallins et granites en Bretagne méridionale: le domaine de l'Anticlinal de Cornouailles, *Mémoire du Service Géologique de la Carte Géologique de France* **1** (1960) 382 pp..

Collot, 1980 B. Collot, Les filons aplito-pegmatitiques du massif du Caroux (Montagne Noire): déformation et mécanismes de mise en place, *Bulletin du BRGM* **2** (1980), pp. 257–267.

Compston et al., 1992 W. Compston, I.S. Williams, J.L. Kirschvink, Z. Zhang and G. Ma, Zircon U–Pb ages for Early Cambrian time scale, *Journal Geological Society London* **149** (1992), pp. 171–184.

Corsini & Rolland, 2009 M. Corsini and Y. Rolland, Late evolution of the southern European Variscan Belt: exhumation of the lower crust in a context of oblique convergence, *Comptes Rendus Geosciences* **341** (2009), pp. 214–223.

Crowley & Ghent, 1999 J.L. Crowley and E.D. Ghent, An electron microprobe study of the U–Th–Pb systematics of metamorphosed monazite: the role of Pb diffusion versus overgrowth and recrystallisation, *Chemical Geology* **157** (1999), pp. 285–302.

Deloule et al., 2001 E. Deloule, M. Chaussidon, M. Glass and C. Koerbel, U–Pb isotopic study of relict zircon inclusions recovered from Muong Nong-type tektites, *Geochimica Cosmochimica Acta* **65** (2001), pp. 1833–1838.

Deloule et al., 2002 E. Deloule, P. Alexendrov, A. Cheilletz, B. Laumonier and P. Barbey, In situ U–Pb zircon ages for early Ordovician magmatism in the Eastern Pyrénées, France: The Canigou orthogneiss, *Geologische Rundschau* **91** (2002), pp. 398–405.

Demange, 1985 M. Demange, The eclogite–facies rocks of the Montagne Noire, France, *Chemical Geology* **50** (1985), pp. 173–188.

Demange et al., 1996 M. Demange, J. Guérangé-Lozes and B. Guérangé, Carte géologique de Lacaune et sa notice, *Carte géologique de la France au 1:50000 n°987, Bureau de Recherches Géologiques et Minières, Orléans, France* (1996).

Denèle et al., 2007 Y. Denèle, P. Olivier, G. Gleizes and P. Barbey, The Hospitalet gneiss dome (Pyrénées) revisited: lateral flow during Variscan transpression in the middle crust, *Terra Nova* **19** (2007), pp. 445–453.

Didier & Lameyre, 1969 J. Didier and J. Lameyre, Les granites du Massif central français: étude comparée des leucogranites et granodiorites, *Contributions to Mineralogy and Petrology* **24** (1969), pp. 219–328.

Ducrot et al., 1979 J. Ducrot, J.R. Lancelot and J. Reille, Datation en Montagne Noire d'une phase majeure d'amincissement rustal caractéristique de l'Europe Varisque, *Bull Soc Géol France* **24** (1979), pp. 501–505.

Duguet et al., 2007 M. Duguet, N. Lebreton and M. Faure, P–T paths reconstruction of a collisional event: the example of the Thiviers–Payzac Unit in the Variscan French Massif Central, *Lithos* **98** (2007), pp. 210–232.

Duthou et al., 1984 J.L. Duthou, J.M. Cantagrel, J. Didier and Y. Vialette, Paleozoïc granitoids from the French Massif Central: age and origin studied by $^{87}Rb/^{87}Sr$ system, *Physics of the Earth and Planetary Interiors* **35** (1984), pp. 131–144.

Echtler & Malavieille, 1990 H. Echtler and J. Malavieille, Extensional tectonics, basement uplift and Stephano–Permian collapse basin in a late Variscan metamorphic core complex (Montagne Noire, southern Massif Central), *Tectonophysics* **177** (1990), pp. 125–138.

Engel et al., 1980 W. Engel, R. Feist and W. Franke, Le Carbonifère anté-stéphanien de la Montagne Noire : rapports entre mise en place des nappes et sédimentation, *Bulletin du BRGM* **2** (1980), pp. 341–389.

Faure, 1995 M. Faure, Late orogenic Carboniferous extensions in the Variscan French Massif Central, *Tectonics* **14** (1995), pp. 132–153

Faure et al., 1997 M. Faure, C. Leloix and J.-Y. Roig, L'évolution polycyclique de la chaîne Hercynienne, *Bulletin de la Société Géologique de France* **168** (1997), pp. 695–705.

Faure et al., 2002 M. Faure, P. Monié, H. Maluski, C. Pin and C. Leloix, Late Visean thermal event in the northern part of the French Massif Central. New $^{40}Ar/^{39}Ar$ and Rb–Sr isotopic constraints on the Hercynian syn-orogenic extension, *International Journal of Earth Science* **91** (2002), pp. 53–75.

Faure et al., 2003 M. Faure, W. Lin, U. Schärer, L. Shu, Y. Sun and N. Arnaud, Continental subduction and exhumation of UHP rocks. Structural and geochronological insights from the Dabieshan (E. China), *Lithos* **70** (2003), pp. 213–241.

Faure et al., 2005 Faure, M., Bé Mézème, E., Duguet, M., Cartier, C., Talbot, J.-Y., 2005. Paleozoic tectonic evolution of Medio-Europa from the example of the French Massif Central and Massif Armoricain. Journal of Virtual Explorer Electronic edition, ISSN 1441-8142 vol. 19, paper 5, 1-21.

Faure et al., 2008 Faure M., Bé Mézème E., Cocherie A., Rossi P., Chemenda A., Boutelier D. 2008. Devonian geodynamic evolution of the Variscan Belt, insights from the French Massif Central and Massif Armoricain, Tectonics, 27, TC2005, http://dx.doi.org/10.1029/2007TC002115 11.

Faure et al., 2009a M. Faure, J.M. Lardeaux and D. Ledru, A review of the pre-Permian geology of the French Massif Central, *Comptes Rendus Géosciences* (2009), pp. 202–213 10.1016/j.crte.2008.12. 001, 202-213.

Faure et al., 2009b M. Faure, E. Bé Mézème, A. Cocherie, J. Melleton and P. Rossi, The South Millevaches Middle Carboniferous crustal melting and its place in the French Variscan Belt, *Bulletin de la Société Géologique de France* **180** (2009), pp. 471–477.

Faure et al., 2010 M. Faure, C. Sommers, J. Melleton, A. Cocherie and O. Lautout, The Léon Domain (French Massif Armoricain): a westward extension of the Mid-German Crystalline Rise? Structural and geochronological insights, *International Journal of Earth Science* **99** (2010), pp. 65–81.

Feist & Galtier, 1985 R. Feist and J. Galtier, Découverte de flores d'âge namurien probable dans le flysch à olistolithes de Cabrières (Hérault). Implications sur la durée de la sédimentation synorogénique dans la Montagne Noire (France Méridionale), *Comptes Rendus de l'Académie des Sciences* **300** (1985), pp. 207–212.

Franke, 2000 W. Franke, The mid-European segment of the Variscides : tectonostratigraphic units, terrane boundaries and plate tectonic evolution. In: W. Franke, V. Haak, O. Oncken and

D. Tanner, Editors, *Orogenic Processes: Quantification and Modelling in the Variscan Belt*, *Geological Society of London, Special Publications* **179** (2000), pp. 35–36.

Gèze, 1949 B. Gèze, Etude géologique de la Montagne Noire et des Cévennes méridionales, *Mémoire de la Société Géologique de France* **62** (1949), pp. 1–215.

Goujou, 1992 Goujou, J. C. 1992. Analyse pétro-structurale dans un avant-pays métamorphique : influence du plutonisme tardi-orogénique varisque sur l'encaissant épi- à mésozonal de Vendée. Documents du BRGM, 216.

Guillot & Ménot, 2009 S. Guillot and R.-P. Ménot, Phanerozoic evolution of the External Crystalline Massifs of the Western Alps, *Comptes Rendus Geosciences* **341** (2009), pp. 253–265

Guillot et al., 2003 S. Guillot, E. Garzanti, D. Baratoux, D. Marquer, G. Mahéo and J. De Sigoyer, Reconstructing the total shortening history of the NW Himalaya, *Geochemistry, Geophysics, Geosystems* 1525-2027 **4** (7) (2003), p. 1064 10.1029/2002GC000484.

Hamet & Allègre, 1976 J. Hamet and C. Allègre, Hercynian orogeny in the Montagne Noire (France). Application of ^{87}Rb–^{87}Sr systematics, *Geological Society of America Bulletin* **87** (1976), pp. 1429–1442.

Harris & Massey, 1994 N. Harris and J. Massey, Decompression and anatexis of Himalayan metapelites, *Tectonics* **13** (1994), pp. 1537–1546.

Johnston & Gutierrez-Alonso, 2010 S. Johnston and G. Gutierrez-Alonso, The North American Cordillera and West European Variscides: contrasting interpretations of similar mountain systems, *Gondwana Research* **17** (2010), pp. 516–525.

Kelsey et al., 2008 D.E. Kelsey, C. Clark and M. Hand, Thermobarometric modelling of zircon and monazite growth in melt-bearing systems: examples using model metapelitic and metapsammitic granulites, *Journal of Metamorphic Geology* **26** (2008), pp. 199–212.

Lardeaux et al., 2001 J.M. Lardeaux, P. Ledru, I. Daniel and S. Duchène, The Variscan French Massif Central — a new addition to the ultra-high pressure metamorphic “club”: exhumation processes and geodynamic consequences, *Tectonophysics* **323** (143–167) (2001), p. 2001.

Le Fort, 1981 P. Le Fort, Manaslu leucogranite: a collision signature in the Himalaya, a model for its genesis and emplacement, *Journal of Geophysical Research* **86** (1981), pp. 10545–10568.

Ledru et al., 1989 P. Ledru, J.-M. Lardeaux, D. Santallier, A. Autran, J.-M. Quenardel, J.-P. Floc'h, G. Lerouge, N. Maillet, J. Marchand and A. Ploquin, Où sont les nappes dans le Massif Central Français?, *Bulletin de la Société Géologique de France* **5** (1989), pp. 605–618.

Ledru et al., 2001 P. Ledru, G. Courrioux, C. Dallain, J.M. Lardeaux, J.M. Montel, O. Vanderhaeghe and G. Vitel, The Velay dome (French Massif Central): melt generation and granite emplacement during orogenic evolution, *Tectonophysics* **342** (2001), pp. 207–237.

Lévêque, 1990 Lévêque, MH. 1990. Contribution de la geochronology U/Pb à la caractérisation du magmatisme cadomien de la partie sud-est du Massif central. Ph. D. thesis, Montpellier Univ., France.

Ludwig, 2003 K.R. Ludwig, ISOPLOT/EX, version 3. A geochronological toolkit for Microsoft Excel, *Berkeley Geochronology Center, Spec. Pub.* **4** (2003) 70 pp..

Maluski et al., 1991 H. Maluski, S. Costa and H. Echtler, Late Variscan tectonic evolution by thinning of earlier thickened crust. An ^{40}Ar–^{39}Ar study of the Montagne Noire, southern Massif Central, France, *Lithos* **26** (1991), pp. 287–304.

Matte, 1991 P. Matte, Accretionary history and crustal evolution of the Variscan Belt in western Europe, *Tectonophysics* **196** (1991), pp. 309–337.

Matte, 2001 P. Matte, The Variscan collage and orogeny (480–290 Ma) and the tectonic definition of the Armorica microplate : a review, *Terra Nova* **13** (2001), pp. 122–128.

Matte et al., 1998 P. Matte, J. Lancelot and M. Mattauer, La zone axiale Hercynienne de la Montagne Noire n'est pas un “metamorphic core complex” extensif mais un anticlinal post-nappe à cœur anatectique, *Geodinamica Acta* **11** (1998), pp. 13–22.

Melleton et al., 2009 J. Melleton, M. Faure and A. Cocherie, Monazite U–Th/Pb chemical dating of the Early Carboniferous syn-kinematic MP/MT metamorphism in the Variscan French Massif Central, *Bulletin de la Société Géologique de France* **180** (2009), pp. 283–292.

Melleton et al., 2010a J. Melleton, A. Cocherie, M. Faure and P. Rossi, Precambrian protoliths and Early Paleozoic magmatism in the French Massif Central: U–Pb data and the North Gondwana connection in the west European Variscan belt, *Gondwana Research* **17** (2010), pp. 13–25

Melleton et al., 2010b J. Melleton, A. Cocherie, M. Faure and P. Rossi, Precambrian protoliths and Early Paleozoic magmatism in the French Massif Central: U–Pb data and the North Gondwana connection in the west European Variscan belt geochronology, *Gondwana Research* **17** (2010), pp. 13–25.

Melleton et al., in review Melleton, J., Oliot, E., Gardien, V. Cordini, M., Rolland, Y., Cocherie, A., Chronology and significance of tectonothermal events in the Maures-Tanneron Massif (South Variscan Belt) by in situ U–Th–Pb dating of monazites. International Journal of Earth Sciences, in review.

Mezger, 2005 J.E. Mezger, Comparison of the western Aston-Hospitalet and the Bossost domes: evidence for polymetamorphism and its implications for the Variscan tectonic evolution of the Axial Zone of the Pyrénées, *Journal of Virtual Explorer* (2005) Electronic edition, ISSN 1441-8142 vol. 19, paper 6.

Montel et al., 1992 J.-M. Montel, C. Marignac, P. Barbey and M. Pichavant, Thermobarometry and granite genesis: the Hercynian low-P, high-T Velay anatectic dome (French Massif central), *Journal of Metamorphic Geology* **10** (1992), pp. 1–15.

Oncken et al., 2006 O. Oncken, D. Hindle, J. Kley, K. Elger, P. Victor and K. Schemman, Deformation of the Central Andean Upper Plate System — facts, fiction, and constraints for plateau models. In: O. Oncken, G. Chong, G. Franz, P. Giese, H.J. Götze, V. Ramos, M. Strecker and P. Wigger, Editors, *The Andes, Active Subduction Orogeny*, Springer (2006), pp. 459–474.

Paris & Robardet, 1990 F. Paris and M. Robardet, Early Paleozoic paleobiogeography of the Variscan regions, *Tectonophysics* **177** (1990), pp. 193–213.

Parrish, 1990 R. Parrish, U–Pb dating of monazite and its application to geological problems, *Canadian Journal of Earth Sciences* **27** (1990), pp. 1431–1450.

Pin & Duthou, 1990 C. Pin and J.L. Duthou, Sources of Hercynian granitoids from the French Massif Central: inferences from Nd isotopes and consequences for crustal evolution, *Chemical Geology* **83** (1990), pp. 281–296.

Pin & Peucat, 1986 C. Pin and J.J. Peucat, Ages des épisodes de métamorphisme paléozoïques dans le Massif central et le Massif armoricain, *Bulletin de la Société Géologique de France* **8** (1986), pp. 461–469.

Pommier et al., 2002 Pommier A., Cocherie A., Legendre O. (2002) EPMA Dating User's manual: Age calculation from electron probe microanalyser measurements of U–Th–Pb. BRGM, 9 pp.

Roger et al., 2004 F. Roger, J.-P. Respaut, M. Brunel, P. Matte and J.-L. Paquette, Première datation U–Pb des orthogneiss oeillés de la zone axiale de la Montagne Noire (sud du Massif Central): nouveaux témoins du magmatisme ordovicien dans la chaîne Varisque, *Comptes Rendus Géoscience* **336** (2004), pp. 19–28.

Roig & Faure, 2000 J.-Y. Roig and M. Faure, La tectonique cisaillante polyphasée du Sud-Limousin, *Bulletin de la Société Géologique de France* **171** (2000), pp. 295–307.

Rossi et al., 2009 P. Rossi, G. Oggiano and A. Cocherie, A restored section of the "southern Variscan real" across the Corsica–Sardinia microcontinent, *Comptes Rendus Geosciences* **341** (2009), pp. 224–238.

Schaltegger et al., 1999 U. Schaltegger, C.M. Fanning, D. Günther, J.C. Maurin, K. Schulmann and D. Gebauer, Growth, annealing and recrystallization of zircon and preservation of monazite in high grade metamorphism: conventional and in-situ U–Pb isotope, cathodoluminescence and microchemical evidence, *Contributions to Mineralogy and Petrology* **134** (1999), pp. 186–201.

Schilling et al., 2006 F. Schilling, R. Trumbull, H. Brasse, C. Haberland, G. Asch, D. Bruhn, K. Mai, V. Haak, P. Giese, M. Munoz, J. Ramelow, A. Rietbock, E. Ricaldi and T. Vietor, Partial melting in the Central Andean Crust: a review of Geophysical, Petrophysical and Petrologic Evidence. In: O. Oncken, G. Chong, G. Franz, P. Giese, H.J. Götze, V. Ramos, M. Strecker and P. Wigger, Editors, *The Andes, Active Subduction Orogeny*, Springer (2006), pp. 459–474.

Schuiling, 1960 Schuiling, R., 1960. Le dôme gneissique de l'Agoût (Tarn et Hérault). Mémoire de la Société Géologique de France, 91.

Schulman et al., 2009 K. Schulman *et al.*, An Andean-type Paleozoic convergence in the Bohemian Massif, *Comptes Rendus Geosciences* **341** (2009), pp. 266–286.

Soula et al., 1986 J.-C. Soula, P. Debat, J. Deramond and P. Pouget, A dynamic model of the structural evolution of the Hercunian Pyrénées, *Tectonophysics* **129** (1986), pp. 29–51.

Soula et al., 2001 J.-C. Soula, P. Debat, S. Brusset, G. Bessière, F. Christophoul and J. Deramond, Thrust-related, diapiric and extensional doming in a frontal orogenic wedge: example of the Montagne Noire, southern French Hercynian belt, *Journal of Structural Geology* **23** (2001), pp. 1677–1699.

Suzuki & Adachi, 1991 K. Suzuki and M. Adachi, Precambrian provenance and Silurian metamorphism of the Tsubonosawa paragneiss in the South Kitakami terrane, Northeast Japan, revealed by the chemical Th–U–total Pb isochron ages of monazite, zircon and xenotime, *Geochemical Journal* **25** (1991), pp. 357–376.

Suzuki & Kato, 2008 K. Suzuki and T. Kato, CHIME dating of monaizte, xenotime, zircon and polycrase: protocol, pitfalls and chemical criterion of possibly discordant age data, *Gondwana Research* **14** (2008), pp. 569–586.

Tait et al., 1997 J. Tait, V. Bachtadse, W. Franke and H.C. Soffel, Geodynamic evolution of the European Variscan fold belt: paleomagnetic and geological constraints, *Geologische Rundschau* **86** (1997), pp. 585–598.

Tera & Wasserburg, 1972 F. Tera and G.J. Wasserburg, U–Th–Pb systematics in three Apollo 14 basalts and the problem of initial Pb in lunar rocks, *Earth and Planetary Science Letters* **14** (1972), pp. 281–304.

Turrillot et al., 2009 P. Turrillot, R. Augier and M. Faure, The top-to-the-East Sarzeau Shear Zone and its place in the syn-orogenic extensional tectonics of Southern Armorica, *Bulletin de la Société Géologique de France* **180** (2009), pp. 247–261.

Van Den Driessche & Brun, 1992 J. Van Den Driessche and J.-P. Brun, Tectonic evolution of the Montagne Noire (French Massif Central): a model of extensional dome, *Geodinamica Acta* **5** (1992), pp. 85–99.

Vissers, 1992 R. Vissers, Variscan extension in the Pyrenees, *Tectonics* **11** (1992), pp. 1369–1384.

Von Raumer et al., 2009 J. Von Raumer, F. Bussy and G. Stampfli, The Variscan evolution in the External Massifs of the Alps and place in their Variscan framework, *Comptes Rendus Geosciences* **341** (2009), pp. 239–252.

Wendt & Carl, 1991 I. Wendt and C. Carl, The statistical distribution of the mean squared weighted deviation, *Chemical Geology* **86** (1991), pp. 275–285.

Whitney et al., 2004 D.L. Whitney, C. Teyssier and C.S. Siddoway, Gneiss domes in orogeny, *Geological Society of America, Special Paper* **380** (2004), p. 393p.

Wiedenbeck et al., 1995 M. Wiedenbeck, P. Allé, F. Corfu, W.L. Griffin, M. Meier, F. Oberli, A. von Quadt, J.C. Roddick and W. Spiegel, Three natural zircon standards for U–Th–Pb, Lu–Hf, trace element and REE analysis, *Geostandards Newsletter* **19** (1995), pp. 1–23.

Williams, 1998 I.S. Williams, U–Th–Pb geochronology by ion microprobe, *Reviews in Economic Geology* **7** (1998), pp. 1–35.

Zhu & O'Nions, 1999 X.K. Zhu and R.K. O'Nions, Zonation of monazite in metamorphic rocks and its implications for high temperature thermochronology: a case study from the Lewisian terrain, *Earth and Planetary Science Letters* **171** (1999), pp. 209–220.

Zwart, 1986 H.J. Zwart, The Variscan orogeny of the Pyrenees, *Tectonophysics* **129** (1986), pp. 9–27.

Figures and Tables

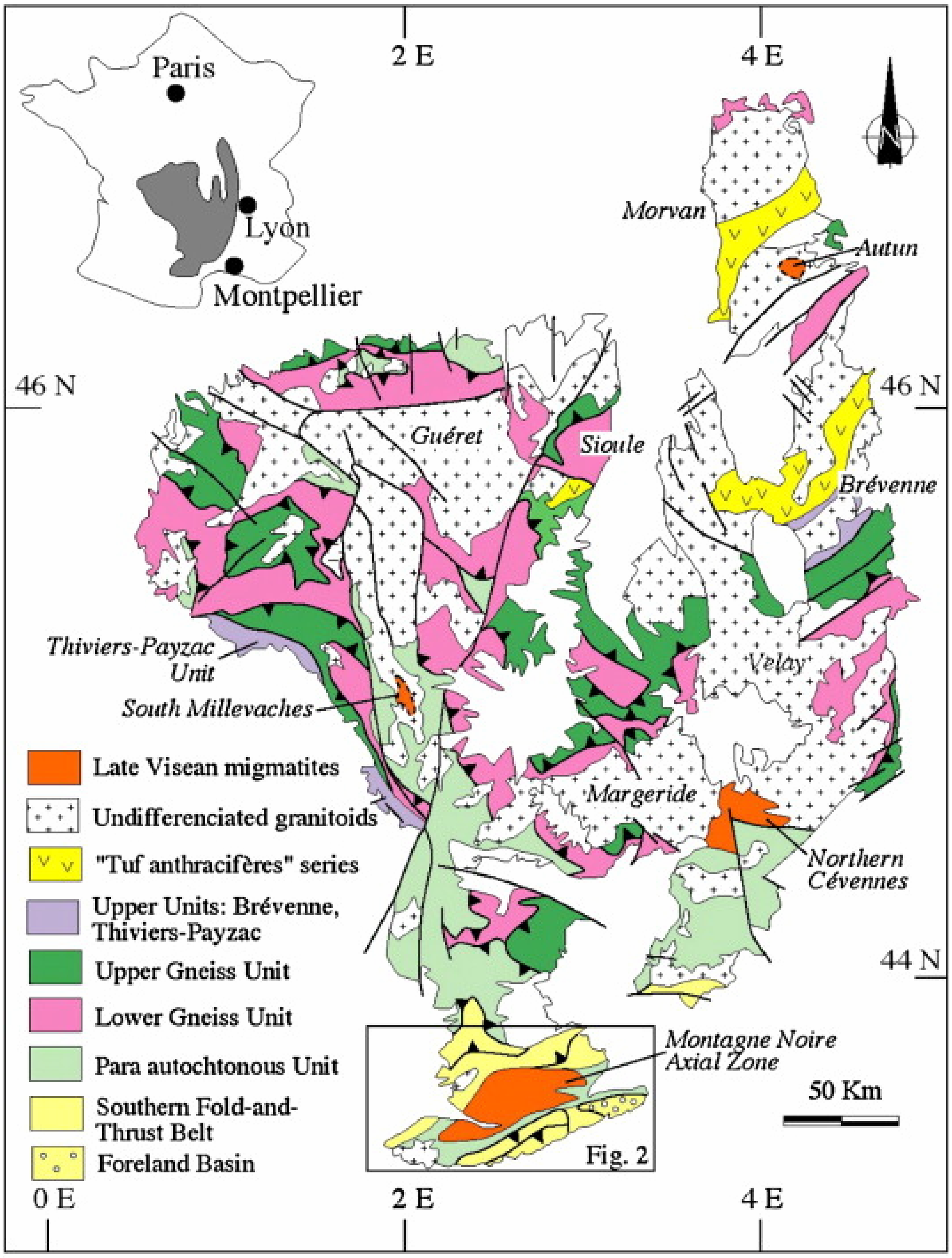

Fig. 1. : Structural map of the Variscan French Massif Central (modified from [Ledru et al., 1989], [Faure et al., 2005], [Faure et al., 2009a] and [Faure et al., 2009b]) showing the location of the Montagne Noire in the southern part of the massif.

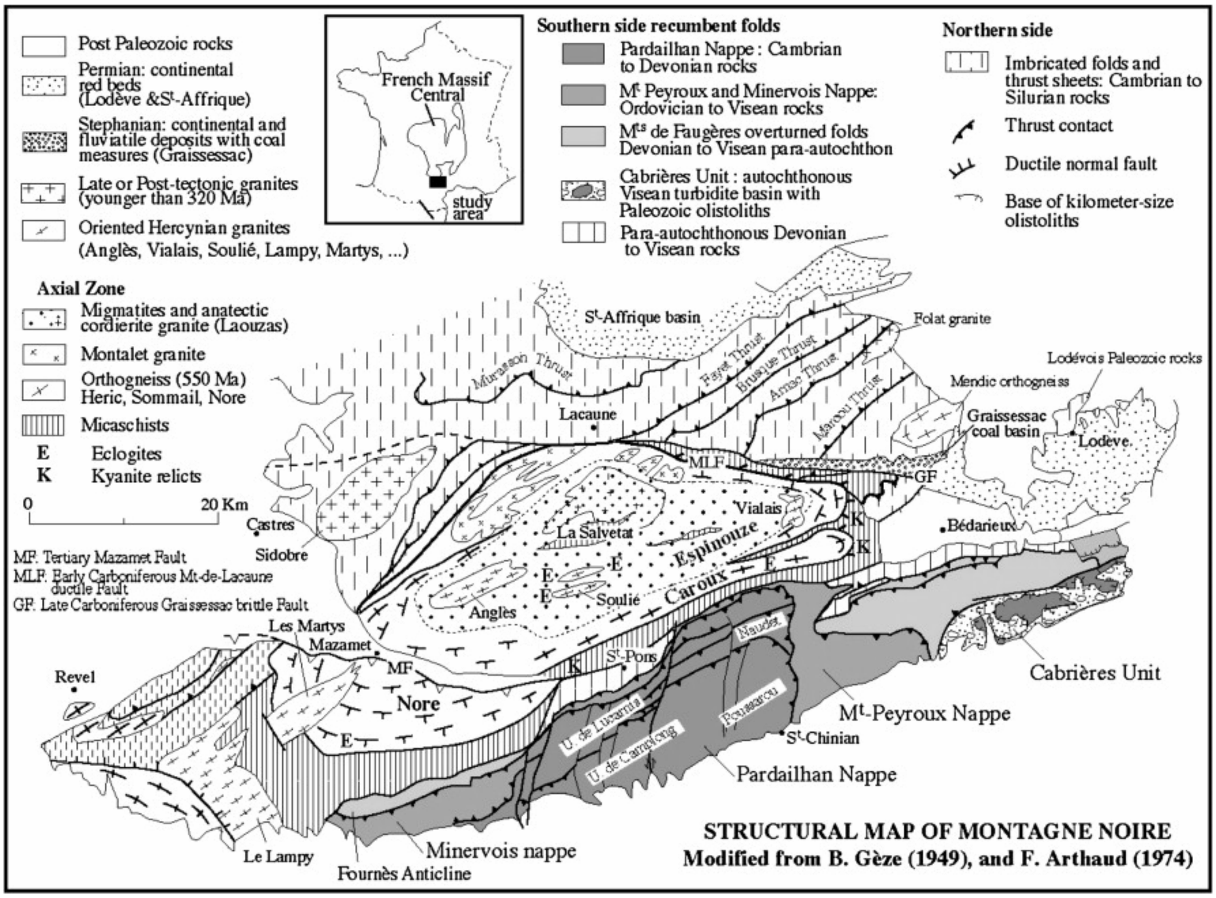

Fig. 2. : Structural map of the Montagne Noire (modified from [Gèze, 1949] and [Arthaud, 1970]). The Montagne Noire is subdivided into a gneissic–migmatitic–granitic axial zone and Paleozoic recumbent folds in the northern and southern flanks.

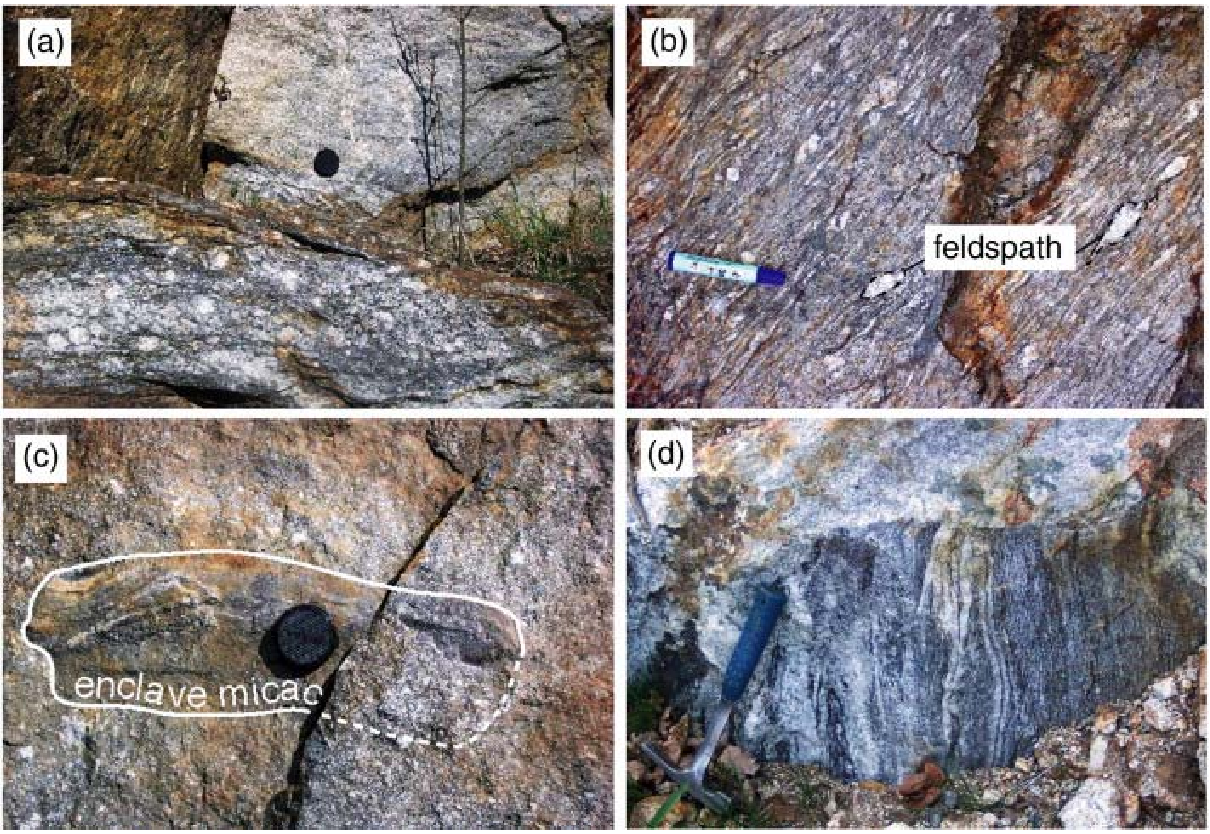

Fig. 3. : Examples of migmatites observed in the Montagne Noire axial zone showing various stages of crustal melting; a: highly melted Ourtigas metatexite; b partially melted Ourtigas orthogneiss with preserved foliation and K-feldspar megacrysts; c: Laouzas anatectic granite with paragneiss enclave oriented in the granite foliation; d: La Salvetat metatexite.

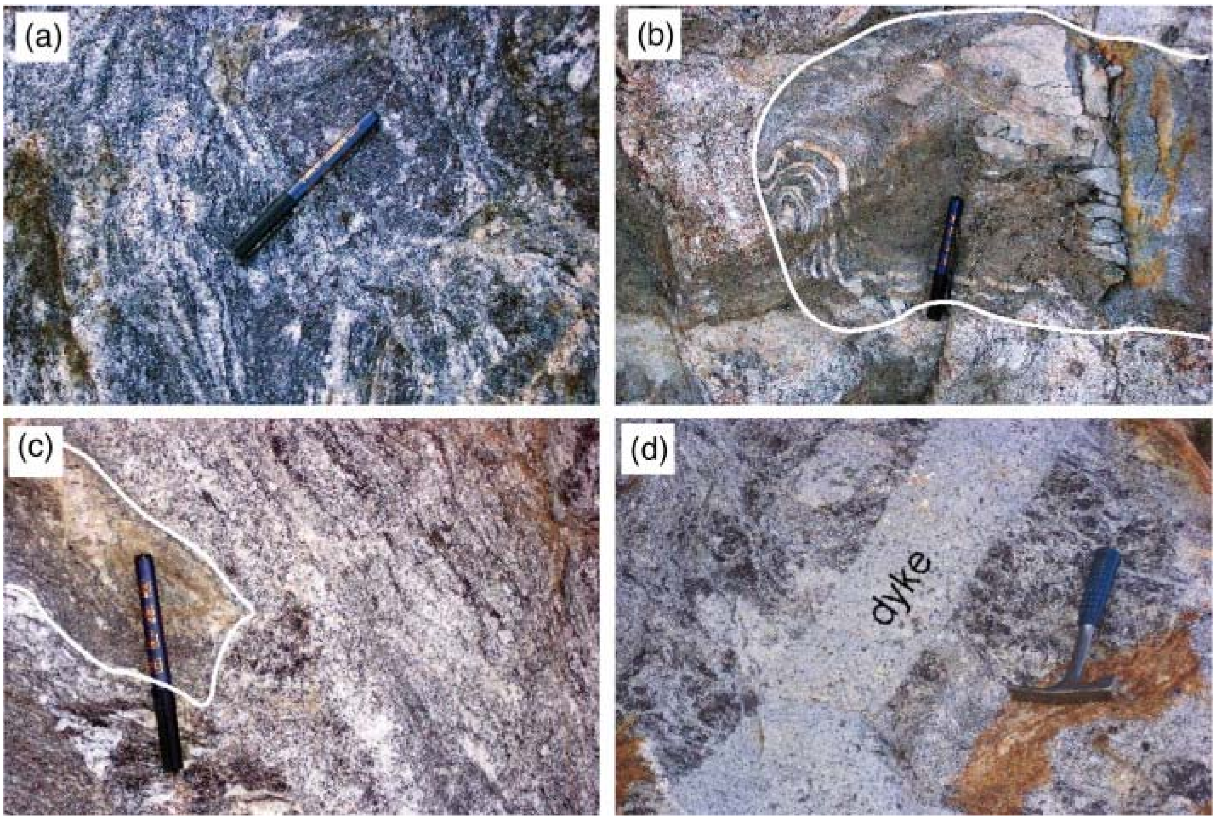

Fig. 4. : Examples of La Salvetat migmatites and anatectic granitoids; a: diatexite; b: Laouzas anatectic granite with metatexite enclave; c: metatexite with paragneiss enclave; d: Laouzas anatectic granitoid cross cut by fine grained aplitic dyke.

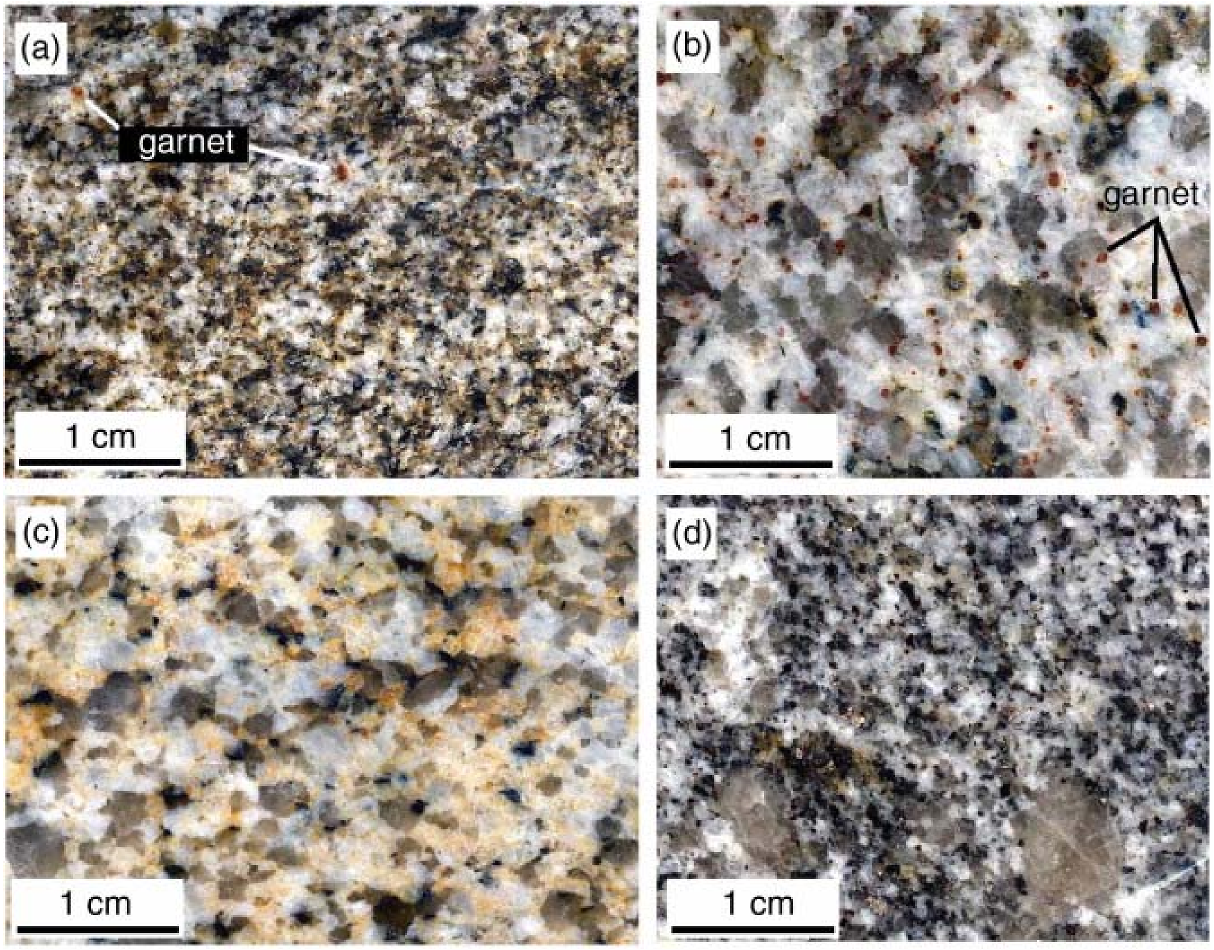

Fig. 5. : Examples of granitoids. a: fine grained Montalet biotite-rich facies with a small amount of garnet; b: medium grained Montalet garnet-rich facies; c: Vialais leucogranite; d: Anglès biotite granite with K-feldspar megacrysts.

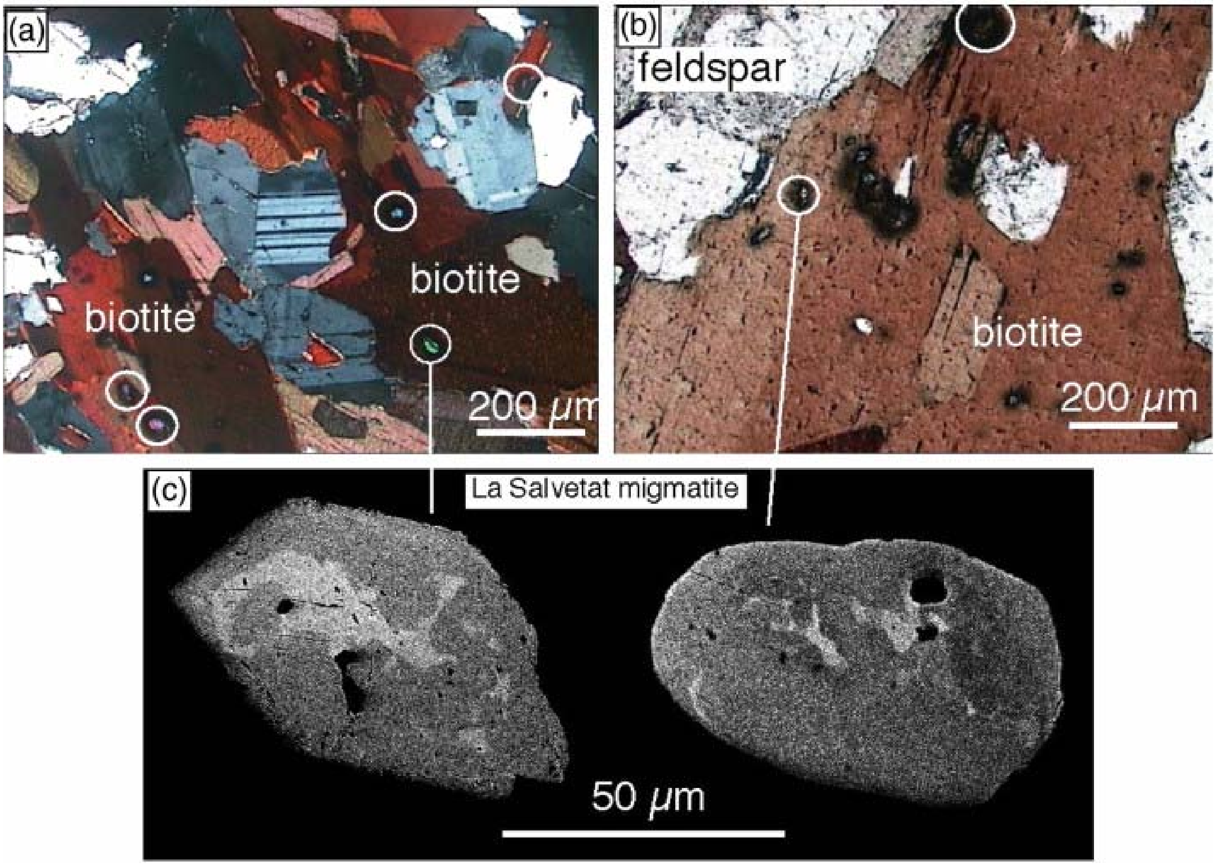

Fig. 6. : Microscopic aspect of La Salvetat migmatite. a: monazite (circled) inclusions in biotite with pleochroic halos, b:detail of monazite inclusions in biotite, c: Back-scattered electron SEM images of monazite grains with subhedral or rounded shapes and patchy zoning, light areas correspond to Th-rich domains.

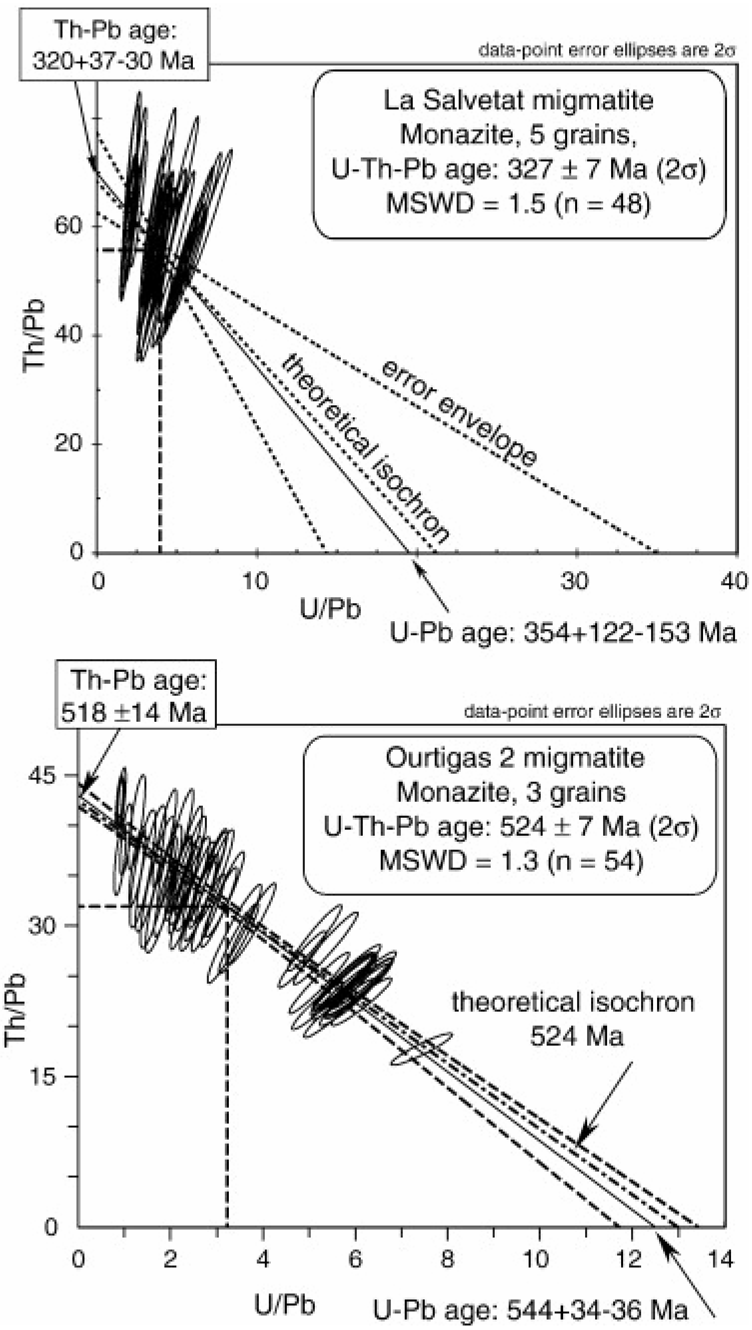

Fig. 7. : U/Th vs. U/Pb isochron diagrams of monazite from La Salvetat and Ourtigas (Ourt 2) migmatites. For each diagram, the regression line is close to the theoretical isochron. The age determined at the intersections of the regression line with the U/Pb and Th/Pb axes support the validity of the calculated age determined at the centroid of the analyses represented by their error ellipse.

Table 1. U–Th–Pb monazite average analyzes.

	Pb (ppm) ±	**U (ppm) ±**	**Th (ppm) ±**	**Th/U ±**	**Isochron age ± 2σ Ma**	***n***
Migmatite						
Ourt1	1945 ± 473	22544 ± 11484	60542 ± 15041	5 ± 4	326 ± 4	29
Ourt1	1403 ± 393	4644 ± 2930	53513 ± 20255	16 ± 10	458 ± 9	30
Ourt2	1639 ± 397	5453 ± 3234	51865 ± 20470	14 ± 11	524 ± 7	54
Espinouse	1980 ± 433	25297 ± 10597	59201 ± 15287	4 ± 3	322 ± 6	36
Salvetat	1023 ± 186	4124 ± 1425	58133 ± 10731	16 ± 7	327 ± 7	48
Granite						
Vialais	2094 ± 425	25148 ± 9335	65922 ± 17006	3 ± 3	320 ± 3	92
Anglès	1106 ± 198	10003 ± 4137	45417 ± 5565	5 ± 2	325 ± 7	56
Montalet-bi	2196 ± 446	9246 ± 7224	68681 ± 10869	19 ± 17	499 ± 6	96
Montalet-gt	937 ± 180	7060 ± 3481	42572 ± 3427	7 ± 3	327 ± 7	58
Laouzas	1133 ± 216	4660 ± 1377	66298 ± 13792	15 ± 5	333 ± 6	54

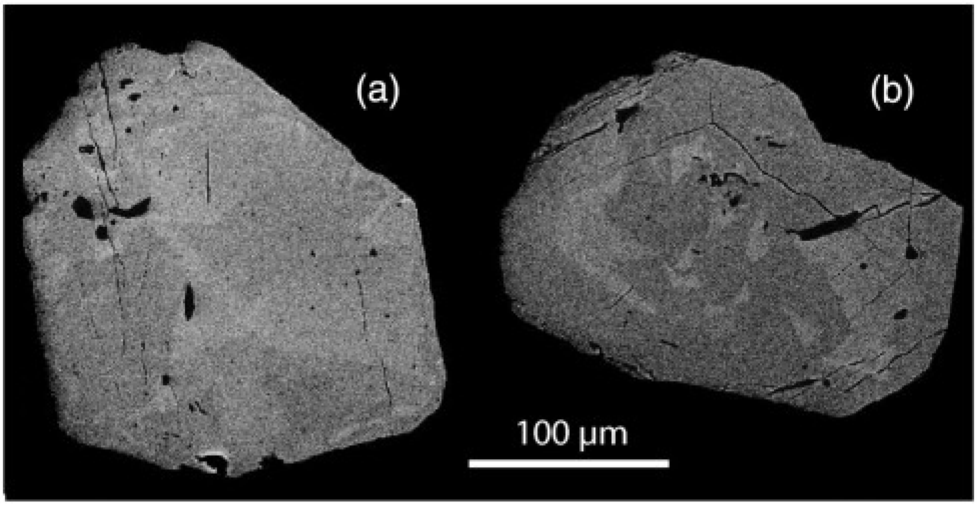

Fig. 8. : Examples of back-scattered electron SEM images of analyzed monazite grains, in the Ourtigas migmatites: a) Ourt 1, b) Ourt 2 samples. The grains exhibit subhedral shapes and patchy zoning, light areas correspond to Th-rich domains.

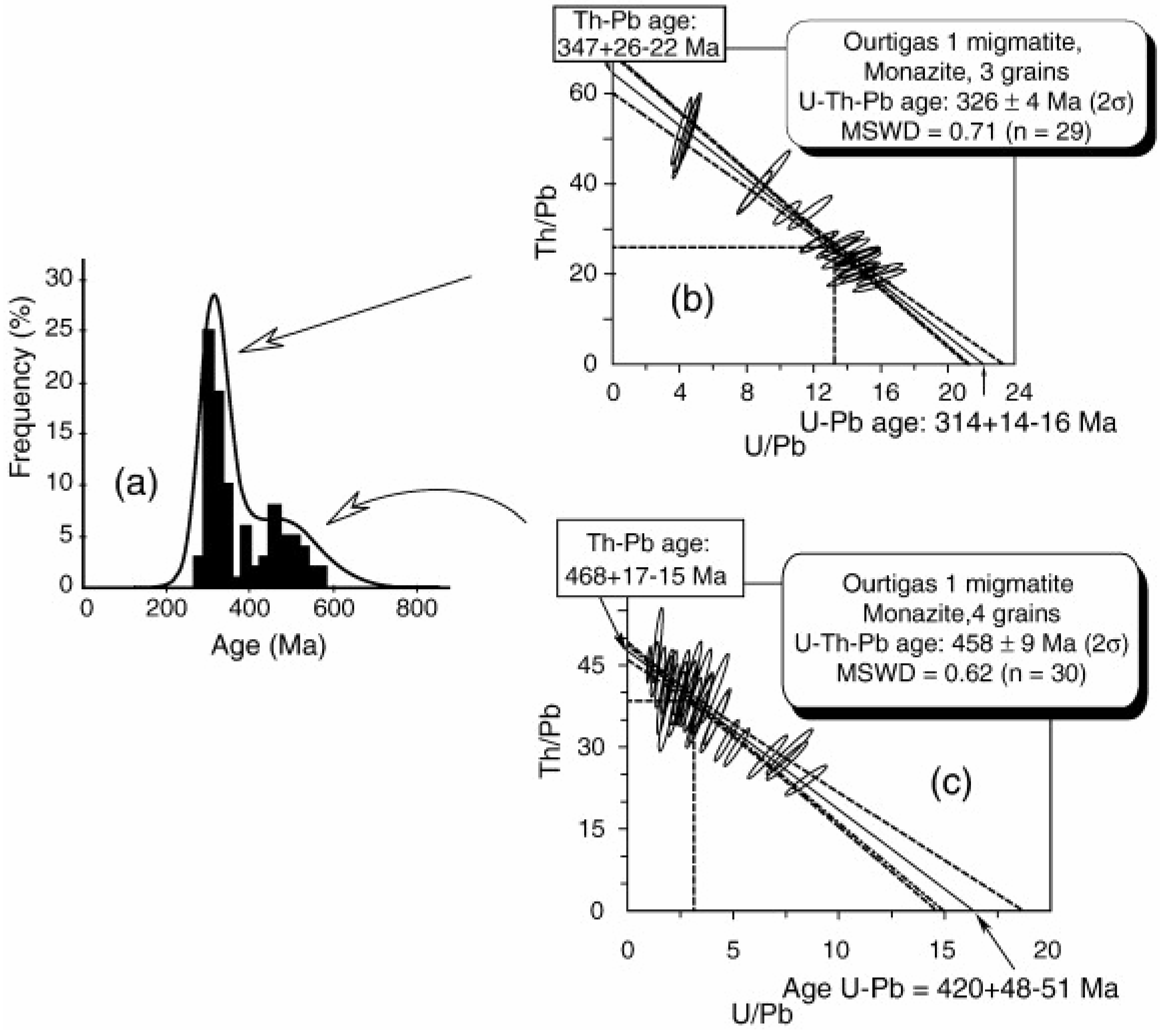

Fig. 9. : Monazite U–Th–Pb dating of the Ourtigas migmatites (Ourt 1). Individual age frequency diagram (a) shows a bimodal distribution. The highest peak corresponds to grains yielding a ca 326 Ma age interpreted as that of partial melting, and the lowest one represents grains yielding a ca 458 Ma age interpreted as that of the orthogneiss protolith (cf. Fig. 3 for outcrop exposure).

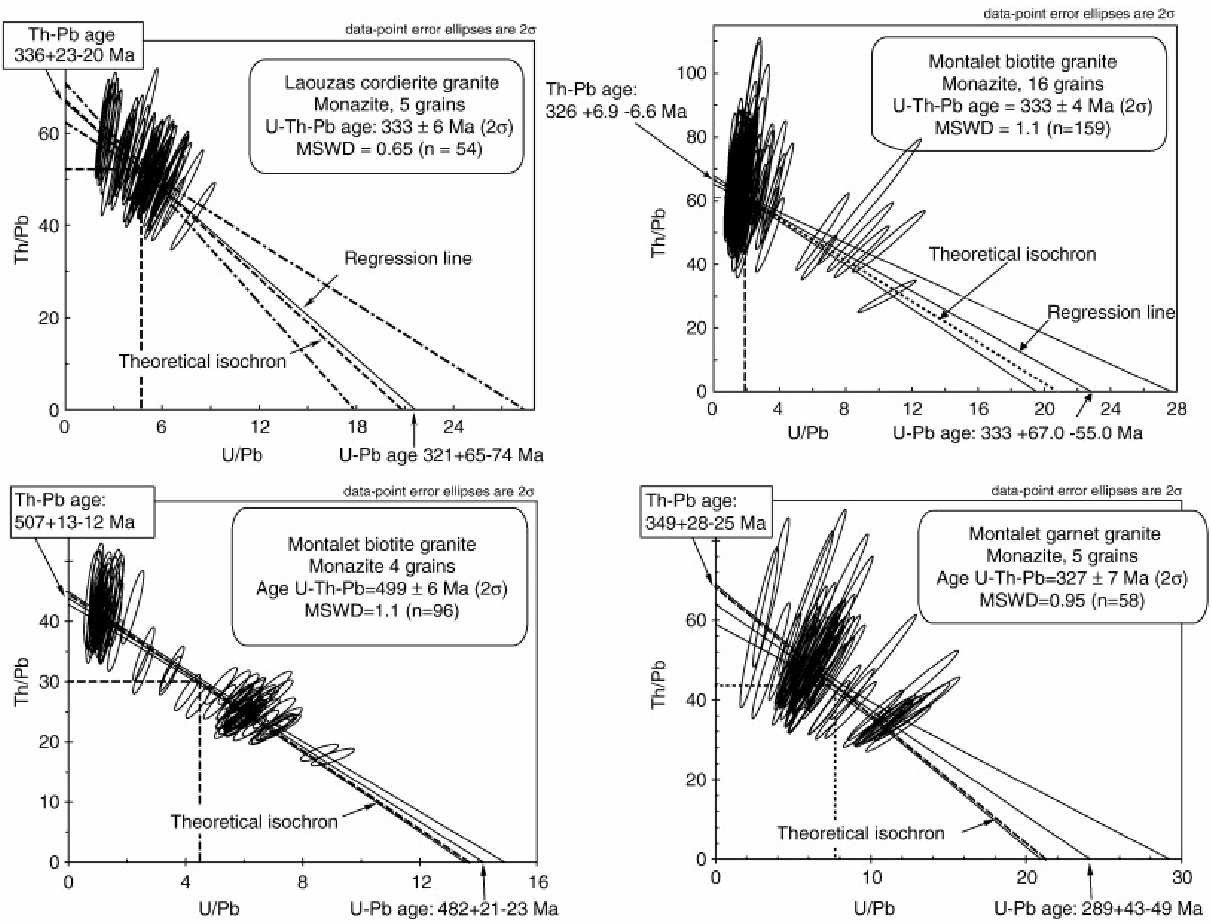

Fig. 10. : U/Th vs. U/Pb isochron diagrams of monazite from Laouzas cordierite granite, and biotite-rich and garnet-rich Montalet granites. For each diagram, the regression line is close to the theoretical isochron. The age determined at the intersections of the regression line with the U/Pb and Th/Pb axes support the validity of the calculated age determined at the centroid of the population. Three ages range around 333–327 Ma, whereas the last age at ca 500 Ma is interpreted as that on inherited grains from the protolih magmatic source.

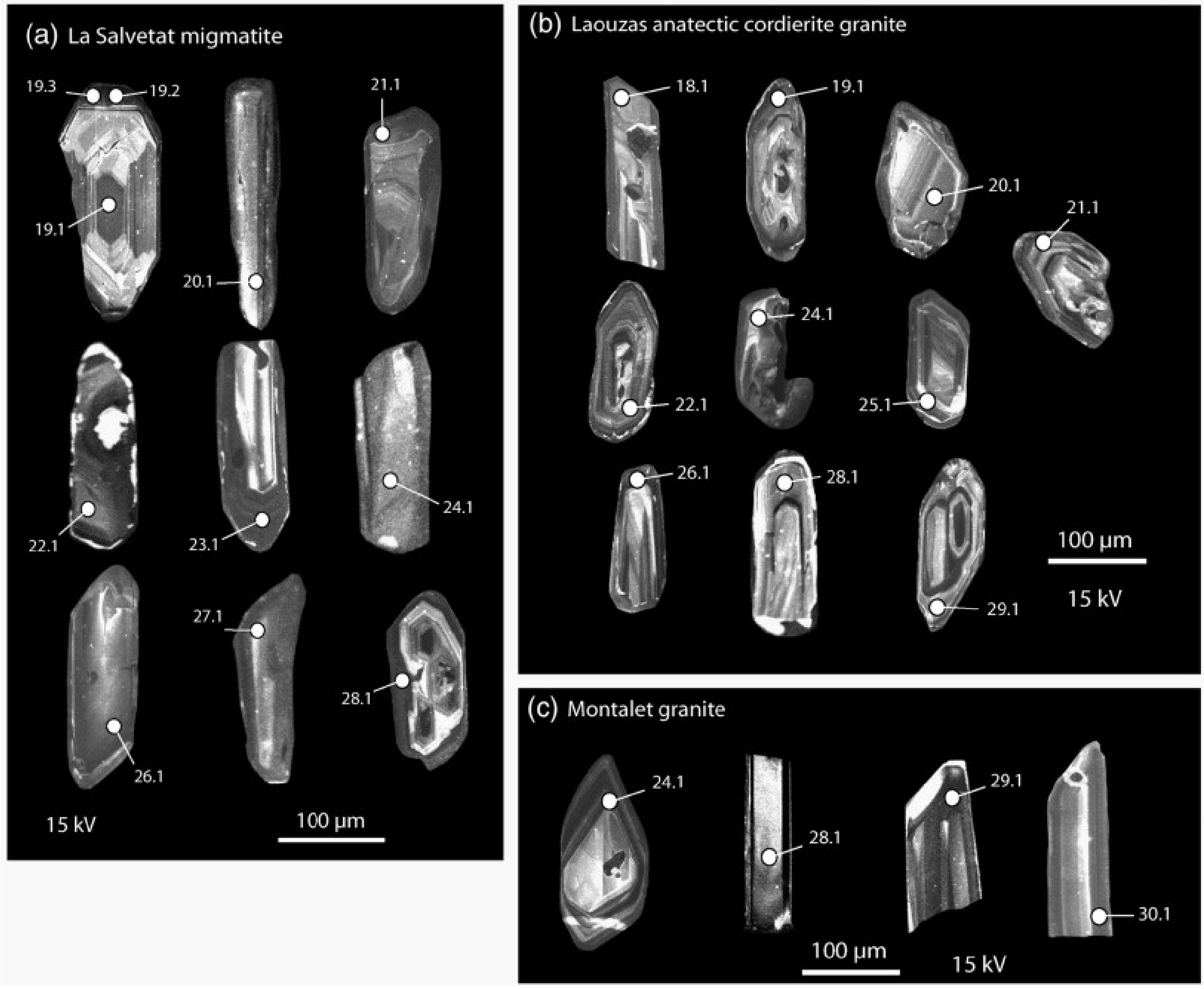

Fig. 11. : Examples of cathodo-luminescence images of the dated zircon. a — La Salvetat migmatites, b — Laouzas cordierite granite, c — Montalet garnet-rich facies. In La Salvetat migmatite and Laouzas granite, most of zircons are euhedral with inherited cores. Numbers for each zircon refer to analytic [Table 2a], [Table 2b], [Table 2c] and [Table 3].

Table 2a. Ion probe results for La Salvetat Migmatite.

							Total				**Radiogenic**		**Age (Ma)**	
Grain spot	**U (ppm)**	**Th (ppm)**	**Th/U**	**$^{206}Pb^{*}$ (ppm)**	**$^{204}Pb/^{206}Pb$**	**f_{206} %**	**$^{238}U/^{206}Pb$**	**±**	**$^{207}Pb/^{206}Pb$**	**±**	**$^{206}Pb/^{238}U$**	**±**	**$^{206}Pb/^{238}U$**	**±**
1.1	375	41	0.11	27	–	0.20	11.725	0.274	0.05957	0.00051	0.08512	0.00199	527	12
2.1	326	44	0.14	26	–	< 0.01	10.906	0.352	0.05846	0.00023	0.09175	0.00296	566	17
2.2	476	73	0.15	36	–	< 0.01	11.272	0.181	0.05786	0.00013	0.08879	0.00143	548	8
4.1	875	91	0.10	64	0.00003	0.14	11.682	0.288	0.05911	0.00041	0.08548	0.00211	529	13
5.1	148	57	0.38	11	–	< 0.01	11.187	0.210	0.05792	0.00028	0.08946	0.00168	552	10
6.1	460	193	0.42	36	–	< 0.01	10.919	0.313	0.05795	0.00030	0.09169	0.00263	566	16
7.1	314	192	0.61	22	–	0.19	12.149	0.426	0.05901	0.00057	0.08216	0.00288	509	17
7.2	137	32	0.23	11	–	0.08	10.419	0.644	0.06028	0.00081	0.09591	0.00592	590	35
8.1	460	54	0.12	36	–	< 0.01	11.062	0.261	0.05839	0.00023	0.09044	0.00213	558	13
9.1	190	155	0.82	15	–	0.02	11.071	0.307	0.05891	0.00028	0.09031	0.00251	557	15
10.1	497	62	0.13	37	–	< 0.01	11.488	0.263	0.05817	0.00024	0.08705	0.00199	538	12
11.1	453	47	0.10	33	–	0.08	11.937	0.231	0.05839	0.00024	0.08370	0.00162	518	10
12.1	291	44	0.15	23	–	0.46	10.971	0.461	0.06265	0.00059	0.09073	0.00381	560	22
12.2	595	11	0.02	26	–	< 0.01	19.992	0.503	0.05243	0.00017	0.05004	0.00126	315	8
12.3	149	46	0.31	11	–	< 0.01	11.500	0.171	0.05810	0.00035	0.08697	0.00129	538	8
13.1	318	73	0.23	25	–	< 0.01	10.901	0.269	0.05889	0.00027	0.09174	0.00227	566	13
15.1	241	45	0.19	18	–	0.00	11.416	0.234	0.05827	0.00030	0.08760	0.00179	541	11
16.1	515	53	0.10	38	–	0.06	11.499	0.277	0.05870	0.00027	0.08691	0.00210	537	12
17.1	272	41	0.15	21	–	< 0.01	11.295	0.218	0.05824	0.00033	0.08856	0.00171	547	10
18.1	280	35	0.13	21	–	0.18	11.494	0.198	0.05965	0.00030	0.08685	0.00150	537	9

							Total				Radiogenic		Age (Ma)	
Grain spot	**U (ppm)**	**Th (ppm)**	**Th/U**	**^{206}Pb* (ppm)**	**^{204}Pb/^{206}Pb**	**f_{206} %**	**^{238}U/^{206}Pb**	**±**	**^{207}Pb/^{206}Pb**	**±**	**^{206}Pb/^{238}U**	**±**	**^{206}Pb/^{238}U**	**±**
19.1	329	419	1.27	27	–	< 0.01	10.629	0.193	0.05838	0.00048	0.09420	0.00171	580	10
19.2	894	12	0.01	38	0.00079	1.34	20.311	0.270	0.06332	0.00066	0.04857	0.00065	306	4
19.3	*508*	*80*	*0.16*	*35*	*0.00001*	*0.03*	*12.395*	*0.110*	*0.05744*	*0.00018*	*0.08066*	*0.00072*	*500*	*4*
20.1	668	69	0.10	44	0.00024	0.42	12.915	0.168	0.06013	0.00015	0.07710	0.00100	479	6
21.1	*447*	*35*	*0.08*	*38*	*0.00024*	*0.07*	*10.041*	*0.278*	*0.06084*	*0.00071*	*0.09952*	*0.00276*	*612*	*16*
22.1	447	36	0.08	29	–	0.36	13.195	0.158	0.05936	0.00022	0.07552	0.00090	469	5
23.1	1182	54	0.05	84	0.00002	0.24	12.023	0.135	0.05960	0.00013	0.08297	0.00093	514	6
24.1	589	35	0.06	43	–	0.08	11.731	0.140	0.05859	0.00016	0.08517	0.00101	527	6
25.1	736	52	0.07	55	0.00001	0.08	11.575	0.138	0.05879	0.00010	0.08632	0.00103	534	6
25.2	675	15	0.02	28	0.00066	0.01	20.684	0.308	0.05252	0.00028	0.04834	0.00072	304	4
25.3	796	73	0.09	63	0.00021	0.17	10.937	0.093	0.06027	0.00027	0.09128	0.00078	563	5
26.1	442	445	1.01	30	0.00031	0.72	12.596	0.164	0.06284	0.00066	0.07882	0.00102	489	6
27.1	661	46	0.07	44	–	0.27	12.965	0.165	0.05884	0.00009	0.07692			

Notes : 1. Uncertainties given at the 1σ level (absolute value).

2. Uncertainty in 91500 reference zircon calibration is included in the above uncertainties.

3. f_{206}% denotes the pourcentage of ^{206}Pb that is common Pb.

4. Correction for common Pb for the U/Pb data has been made using the measured ^{238}U/^{206}Pb and ^{207}Pb/^{206}Pb ratios following Tera and Wasserburg (1972) as outlined in Williams (1998).

5. Analyses not included in age calculations are shown in italics.

*Radiogenic Pb due to ^{238}U disintegration.

Table 2b. Ion probe results for Montalet granite.

							Total				**Radiogenic**		**Age (Ma)**	
Grain spot	**U (ppm)**	**Th (ppm)**	**Th/U**	**^{206}Pb* (ppm)**	**^{204}Pb/^{206}Pb**	**f_{206} %**	**^{238}U/^{206}Pb**	**±**	**^{207}Pb/^{206}Pb**	**±**	**^{206}Pb/^{238}U**	**±**	**^{206}Pb/^{238}U**	**±**
4.1	2043	417	0.20	89	0.00020	1.56	19.354	0.193	0.06545	0.00082	0.05086	0.00051	320	3
6.1	*468*	*31*	*0.07*	*28*	–	*0.10*	*14.242*	*0.199*	*0.05645*	*0.00022*	*0.07014*	*0.00098*	*437*	*6*
9.1	4251	3073	0.72	188	0.00186	3.58	18.750	0.266	0.08250	0.00321	0.05142	0.00073	323	4
10.1	2356	1318	0.56	105	–	< 0.01	19.322	0.195	0.05271	0.00012	0.05177	0.00052	325	3
11.1	*2053*	*1059*	*0.52*	*88*	*0.00005*	*0.02*	*19.935*	*0.201*	*0.05287*	*0.00011*	*0.05015*	*0.00050*	*315*	*3*
12.1	*844*	*361*	*0.43*	*35*	–	*0.07*	*20.812*	*0.263*	*0.05292*	*0.00009*	*0.04802*	*0.00061*	*302*	*4*
12.3	*638*	*276*	*0.43*	*27*	–	*0.09*	*20.535*	*0.245*	*0.05317*	*0.00049*	*0.04865*	*0.00058*	*306*	*4*
14.1	1525	556	0.36	66	0.00105	2.01	19.450	0.266	0.06897	0.00474	0.05038	0.00069	317	4
15.1	333	54	0.16	21	–	0.10	13.680	0.144	0.05685	0.00037	0.07303	0.00077	454	5
15.2	468	24	0.05	30	–	0.05	13.212	0.173	0.05688	0.00023	0.07565	0.00099	470	6
16.1	2128	670	0.31	95	0.00108	2.26	18.714	0.195	0.07134	0.00072	0.05223	0.00054	328	3
17.1	433	214	0.49	19	0.00001	7.16	18.324	0.210	0.11087	0.00153	0.05067	0.00058	319	4
18.1	*845*	*32*	*0.04*	*36*	*0.00034*	*0.20*	*20.324*	*0.236*	*0.05415*	*0.00034*	*0.04911*	*0.00057*	*309*	*3*
19.1	*187*	*109*	*0.58*	*27*	–	*0.14*	*6.050*	*0.078*	*0.07322*	*0.00032*	*0.16505*	*0.00213*	*985*	*12*
20.1	*1159*	*19*	*0.02*	*115*	*0.00057*	*2.19*	*8.467*	*0.110*	*0.08134*	*0.00381*	*0.11552*	*0.00149*	*705*	*9*
21.2	*223*	*104*	*0.47*	*17*	–	*0.17*	*11.330*	*0.156*	*0.05983*	*0.00038*	*0.08811*	*0.00121*	*544*	*7*
23.	283	25	0.0	18	0.0006	1.68	13.59	0.1	0.0697	0.00	0.072	0.00	450	5

							Total				Radiogenic		Age (Ma)	
Grain spot	**U (ppm)**	**Th (ppm)**	**Th/U**	**^{206}Pb* (ppm)**	**^{204}Pb/^{206}Pb**	**f_{206} %**	**^{238}U/^{206}Pb**	**±**	**^{207}Pb/^{206}Pb**	**±**	**^{206}Pb/^{238}U**	**±**	**^{206}Pb/^{238}U**	**±**
1			9		8		3	55	0	045	33	083		
23.2	192	41	0.21	12	–	0.16	13.501	0.250	0.05751	0.00036	0.07395	0.00137	460	8
24.1	*653*	*26*	*0.04*	*30*	*0.00005*	*0.62*	*18.519*	*0.186*	*0.05822*	*0.00021*	*0.05366*	*0.00054*	*337*	*3*
25.1	*1412*	*1209*	*0.86*	*143*	*0.00000*	*< 0.01*	*8.462*	*0.071*	*0.06296*	*0.00027*	*0.11823*	*0.00099*	*720*	*6*
26.1	2615	94	0.04	118	0.00011	0.29	18.983	0.209	0.05538	0.00041	0.05253	0.00058	330	4
27.1	*2095*	*7*	*0.00*	*103*	*0.00001*	*0.24*	*17.557*	*0.201*	*0.05556*	*0.00020*	*0.05682*	*0.00065*	*356*	*4*
28.1	*557*	*167*	*0.30*	*23*	*–*	*0.27*	*20.730*	*0.225*	*0.05462*	*0.00053*	*0.04811*	*0.00052*	*303*	*3*
29.1	939	432	0.46	42	–	0.05	19.268	0.176	0.05330	0.00015	0.05188	0.00047	326	3
30.1	424	202	0.48	19	0.00002	0.13	19.428	0.230	0.05391	0.00050	0.05141			

Notes : 1. Uncertainties given at the 1σ level (absolute value).

2. Uncertainty in 91500 reference zircon calibration is included in the above uncertainties.

3. f_{206}% denotes the pourcentage of ^{206}Pb that is common Pb.

4. Correction for common Pb for the U/Pb data has been made using the measured ^{238}U/^{206}Pb and ^{207}Pb/^{206}Pb ratios following Tera and Wasserburg (1972) as outlined in Williams (1998).

5. Analyses not included in age calculations are shown in italics.

Table 2c. Ion probe results for Lauzas granite.

							Total				**Radiogenic**		**Age (Ma)**	
Grain spot	**U (ppm)**	**Th (ppm)**	**Th/U**	**^{206}Pb* (ppm)**	**^{204}Pb/^{206}Pb**	**f_{206} %**	**^{238}U/^{206}Pb**	**±**	**^{207}Pb/^{206}Pb**	**±**	**^{206}Pb/^{238}U**	**±**	**^{206}Pb/^{238}U**	**±**
1.1	318	72	0.23	23	–	0.13	11.700	0.266	0.05899	0.00033	0.08536	0.00194	528	12
2.1	493	66	0.13	37	0.000006	0.06	11.324	0.272	0.05893	0.00023	0.08825	0.00212	545	13
3.1	783	6	0.01	32	–	0.04	20.737	0.532	0.05277	0.00022	0.04820	0.00124	303	8
3.3	272	71	0.26	20	–	0.18	11.677	0.231	0.05943	0.00024	0.08549	0.00169	529	10
4.1	505	60	0.12	38	–	0.09	11.272	0.177	0.05924	0.00022	0.08863	0.00139	547	8
5.1	370	77	0.21	28	0.000090	0.14	11.445	0.295	0.05944	0.00044	0.08725	0.00225	539	13
6.1	334	32	0.09	23	–	0.17	12.333	0.286	0.05870	0.00037	0.08094	0.00188	502	11
7.1	177	51	0.29	14	0.000174	0.07	11.242	0.257	0.05906	0.00025	0.08889	0.00203	549	12
8.1	352	72	0.20	26	–	0.10	11.630	0.288	0.05887	0.00031	0.08590	0.00213	531	13
9.1	661	71	0.11	50	–	0.06	11.457	0.300	0.05878	0.00023	0.08723	0.00228	539	14
10.1	237	42	0.18	17	–	0.16	11.809	0.210	0.05913	0.00031	0.08455	0.00150	523	9
12.1	363	80	0.22	28	–	< 0.01	11.325	0.253	0.05826	0.00030	0.08832	0.00198	546	12
13.1	534	4	0.01	22	0.001203	1.95	20.779	0.319	0.06801	0.00167	0.04719	0.00072	297	4
13.2	96	40	0.41	8	0.000084	< 0.01	10.661	0.273	0.05890	0.00043	0.09385	0.00240	578	14
14.1	282	31	0.11	21	–	0.07	11.334	0.303	0.05901	0.00043	0.08817	0.00235	545	14
14.2	448	94	0.21	35	–	< 0.01	10.940	0.167	0.05856	0.00012	0.09145	0.00139	564	8
15.1	166	39	0.23	13	–	< 0.01	10.883	0.234	0.05850	0.00039	0.09194	0.00198	567	12

							Total				Radiogenic		Age (Ma)	
Grain spot	**U (ppm)**	**Th (ppm)**	**Th/U**	**^{206}Pb* (ppm)**	**^{204}Pb/^{206}Pb**	**f_{206} %**	**^{238}U/^{206}Pb**	**±**	**^{207}Pb/^{206}Pb**	**±**	**^{206}Pb/^{238}U**	**±**	**^{206}Pb/^{238}U**	**±**
16.1	359	47	0.13	27	–	0.03	11.290	0.143	0.05868	0.00029	0.08855	0.00112	547	7
16.2	420	34	0.08	32	0.000080	0.31	11.321	0.187	0.06091	0.00038	0.08806	0.00145	544	9
16.3	447	32	0.07	32	–	0.14	12.086	0.218	0.05868	0.00026	0.08263	0.00149	512	9
17.1	773	90	0.12	58	–	0.12	11.469	0.253	0.05922	0.00020	0.08709	0.00192	538	11
18.1	344	33	0.10	26	–	0.02	11.470	0.137	0.05839	0.00020	0.08717	0.00104	539	6
19.1	651	69	0.11	48	0.000045	0.14	11.622	0.149	0.05924	0.00020	0.08592	0.00110	531	7
20.1	241	163	0.67	19	0.000039	0.38	11.045	0.133	0.06185	0.00022	0.09019	0.00109	557	6
21.1	471	80	0.17	37	0.000062	< 0.01	10.874	0.137	0.05838	0.00018	0.09203	0.00116	568	7
22.1	742	77	0.10	52	0.000182	0.31	12.176	0.175	0.05997	0.00021	0.08187	0.00117	507	7
23.1	531	66	0.12	39	0.000098	0.12	11.567	0.138	0.05909	0.00018	0.08635	0.00103	534	6
24.1	577	74	0.13	41	0.000035	0.11	12.233	0.139	0.05825	0.00024	0.08166	0.00093	506	6
25.1	477	70	0.15	34	0.000141	0.10	11.985	0.139	0.05845	0.00035	0.08335	0.00097	516	6
26.1	1041	67	0.06	76	0.000047	0.16	11.800	0.133	0.05917	0.00011	0.08461	0.00096	524	6
28.1	481	31	0.06	37	–	< 0.01	11.085	0.144	0.05814	0.00031	0.09027	0.00117	557	7
29.1	321	92	0.29	24	–	< 0.01	11.465	0.222	0.05783	0.00051	0.08726			

Notes : 1. Uncertainties given at the 1σ level (absolute value).

2. Uncertainty in 91500 reference zircon calibration is included in the above uncertainties.

3. f_{206}% denotes the pourcentage of ^{206}Pb that is common Pb.

4. Correction for common Pb for the U/Pb data has been made using the measured $^{238}U/^{206}Pb$ and $^{207}Pb/^{206}Pb$ ratios following Tera and Wasserburg (1972) as outlined in Williams (1998).

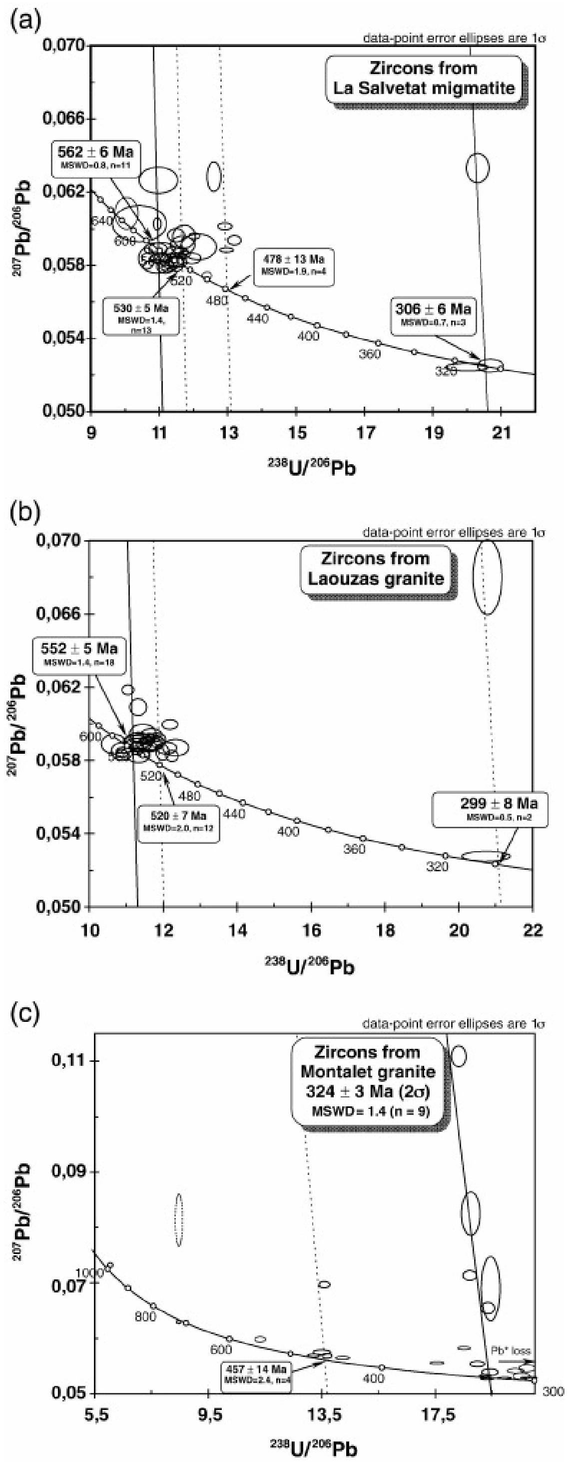

Fig. 12. : Tera–Wasserburg diagrams of zircons U–Pb ages for a) La Salvetat migmatites, b) Laouzas cordierite granite, and c) Montalet biotite-rich facies. For the La Salvetat migmatite, the ca 562 Ma age calculated for 11 analyses represents that of inherited grains from the protolith. The 306 Ma age is poorly constrained by only 3 spot analyses. For the Laouzas cordierite granite, the ca 552 Ma age calculated for 18 analyses represents that of inherited grains from the protolith. The ca 300 Ma age calculated for 2 grains only is geologically

discutable as it is younger than the younger granites (cf Fig. 15) intruding into the Laouzas anatectic granite. For the Montalet granite, 324 Ma age calculated for is interpreted as the granite emplacement age, 457 ± 14 Ma age corresponds to inherited grains from the source of the granitic magma.

Table 3. Inherited zircons in La Salvetat migmatite and Montalet granite.

							Radiogenic Ratios							**Age(Ma)**						
Grain spot	**U (ppm)**	**Th (ppm)**	**Th/U**	**^{206}Pb* (ppm)**	**^{204}Pb/^{206}Pb**	***f*$_{206}$ %**	**^{206}Pb/^{238}U**	**±**	**^{207}Pb/^{235}U**		**^{207}Pb/^{206}Pb**	**±**	**ρ**	**^{206}Pb/^{238}U**	**±**	**^{207}Pb/^{235}U**	**±**	**^{207}Pb/^{206}Pb**	**±**	**% Conc**
La Salvetat migmatite																				
28.1	111	32	0.29	19	–	0.00	0.1988	0.0047	4.158	0.124	0.1517	0.0185	0.787	1169	25	1666	24	2365	31	49
Montalet granite																				
8.1	138	64	0.46	52	–	0.00	0.4507	0.0050	11.007	0.192	0.1771	0.0136	0.628	2398	22	2524	16	2626	22	91
8.2	94	35	0.38	39	–	0.00	0.4861	0.0088	12.420	0.483	0.1853									

Notes : 1. Uncertainties given at the one σ level.

2. f_{206}% denotes the percentage of ^{206}Pb that is common Pb.

3. Correction for common Pb made using the measured ^{204}Pb/^{206}Pb ratio.

4. For % Conc. 100% denotes a concordant analysis.

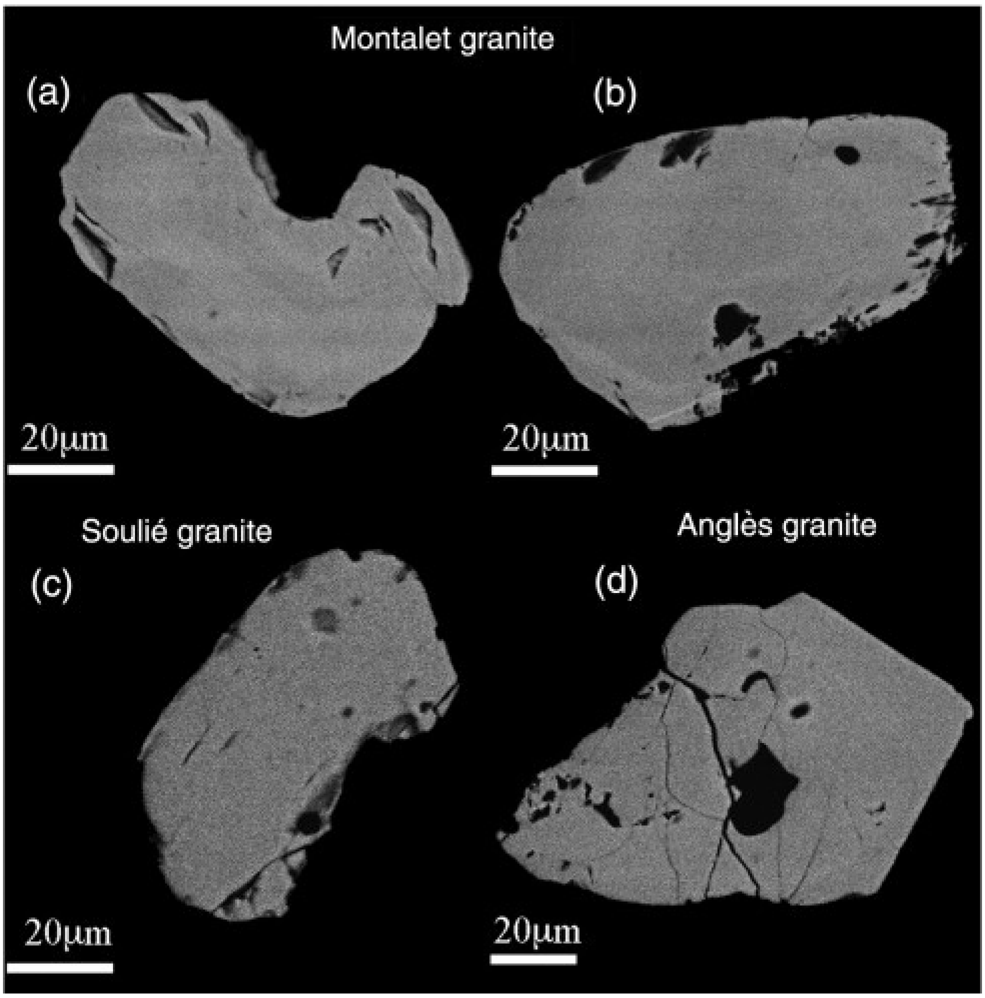

Fig. 13. : Examples of back-scattered electron SEM images of analyzed monazite grains,in the Montalet granite and late migmatitic granites. a) montalet biotite-rich facies, b) Montalet garnet-rich facies, c) Soulié two-micas granite, d) Anglès biotite granite. The grains exhibit subhedral shapes with a faint patchy zoning, and rare inclusions. Light areas correspond to Th-rich domains.

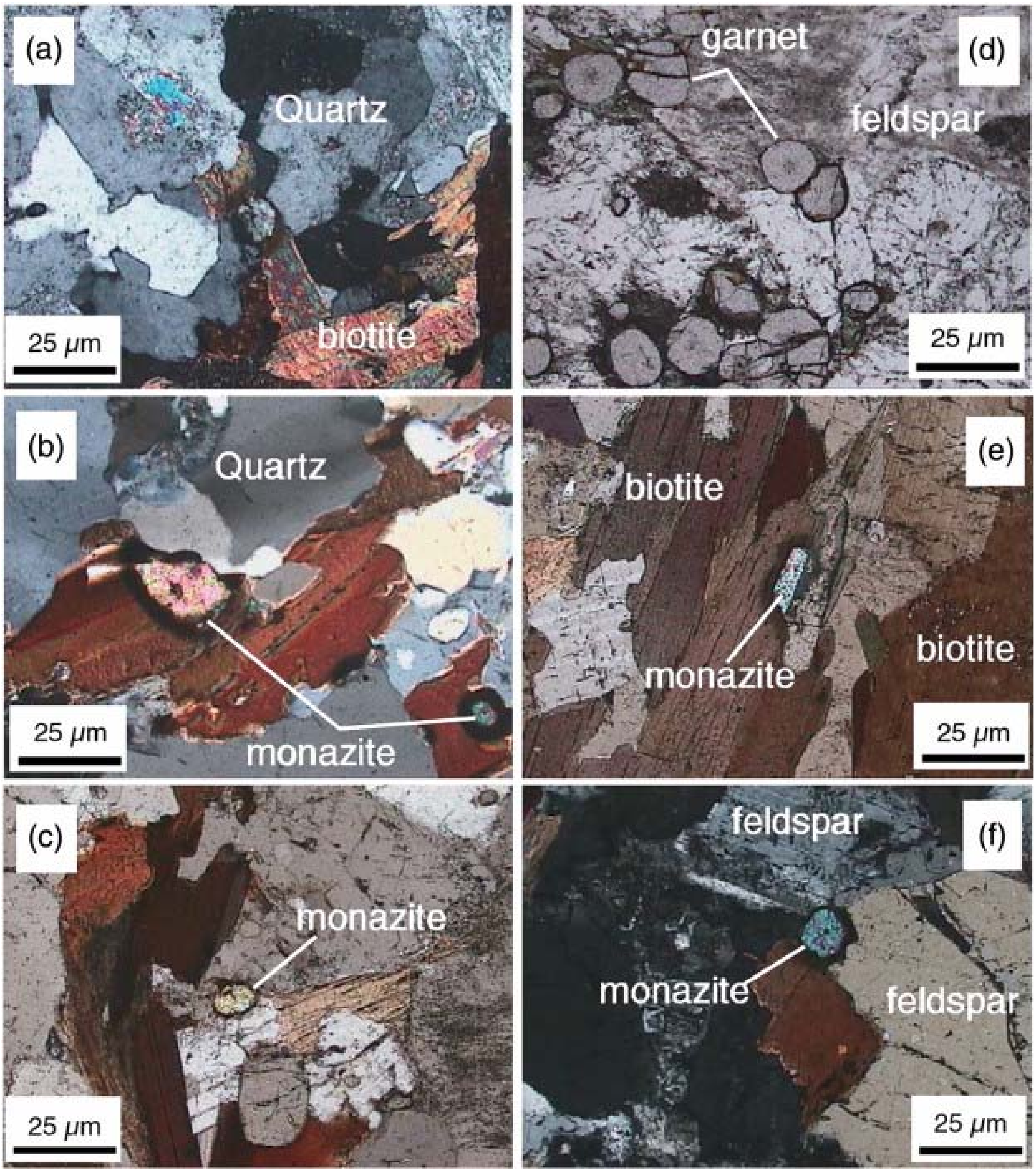

Fig. 14. : Thin sections of Montalet granite showing the textural relationships of monazite with other granite mineral phases. a, b,c: biotite-rich facies; c,d,e: garnet rich facies. Monazite is located either as inclusion in biotite (b, e), or as interstitial phase close to biotite (c) and K-feldspar (d).

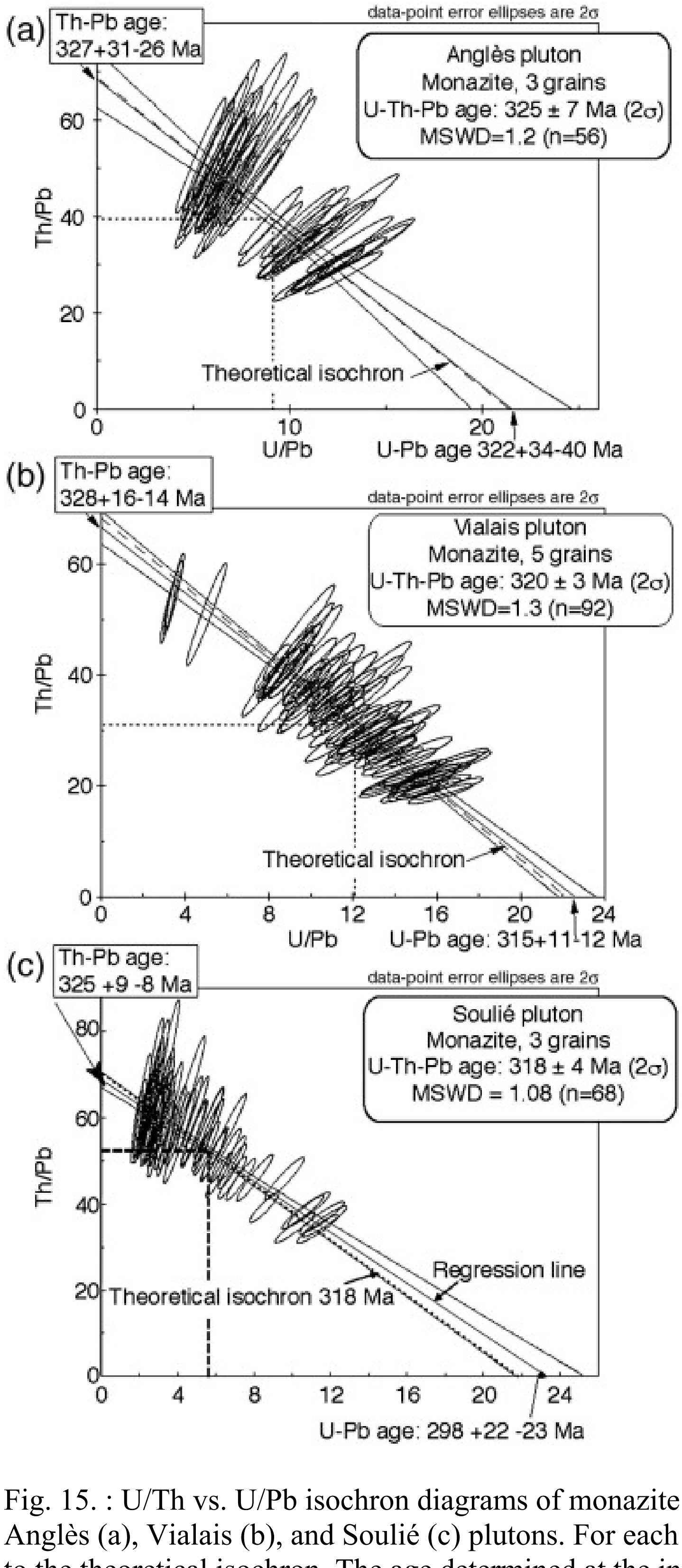

Fig. 15. : U/Th vs. U/Pb isochron diagrams of monazite from late migmatitic granitoids of Anglès (a), Vialais (b), and Soulié (c) plutons. For each diagram, the regression line is close to the theoretical isochron. The age determined at the intersections of the regression line with the U/Pb and Th/Pb axes support the validity of the calculated age determined at the centroid of the population. The three ages, ranging from 325 to 318 Ma, are in good agreement with field observations that show these plutons post-dating the migmatite.

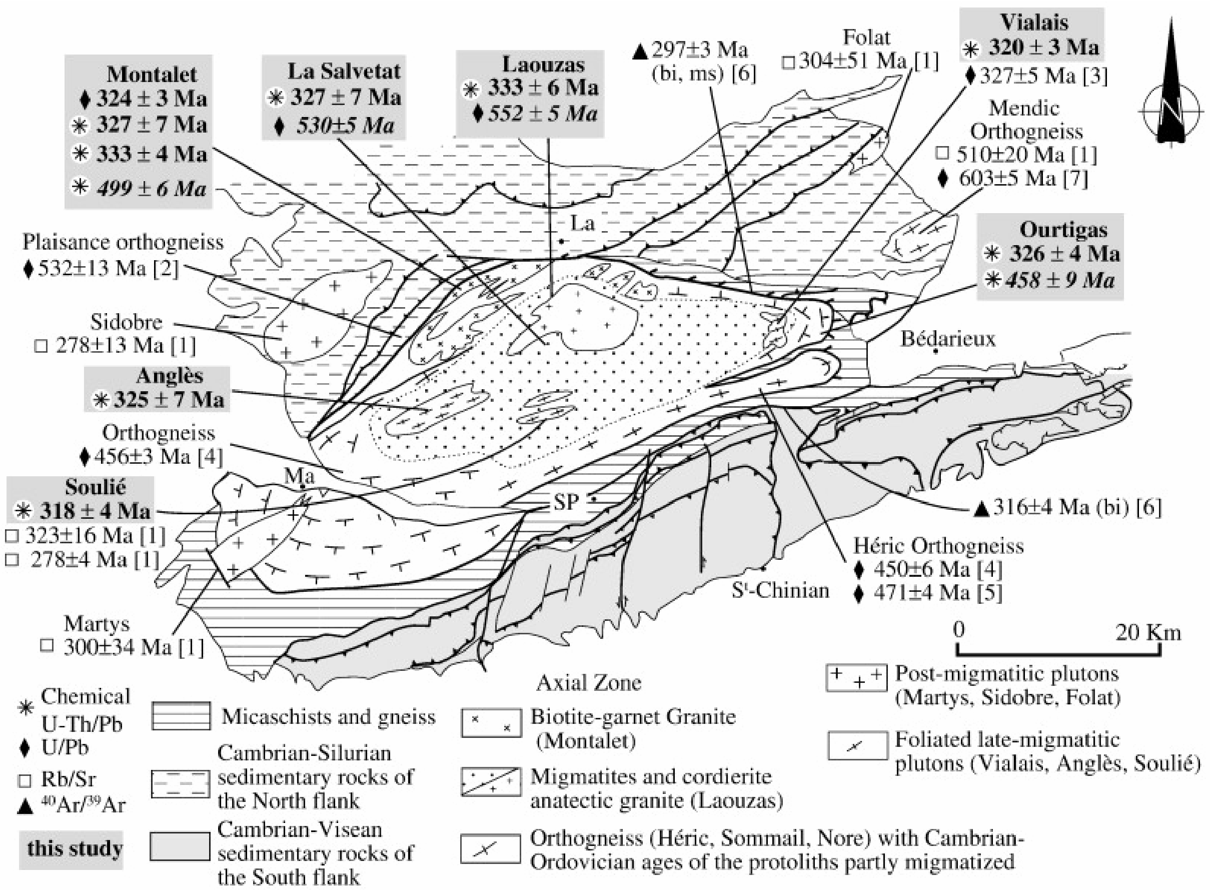

Fig. 16.

Synthetic map of the available radiometric ages for the Axial Zone of the Montagne Noire. [1]: Hamet and Allègre (1976); [2]: Ducrot et al. (1979); [3]: Matte et al. (1998); [4]: Cocherie et al. (2005b); [5]: Roger et al. (2004); [6]: Maluski et al. (1991); [7]: Lévêque, 1990.

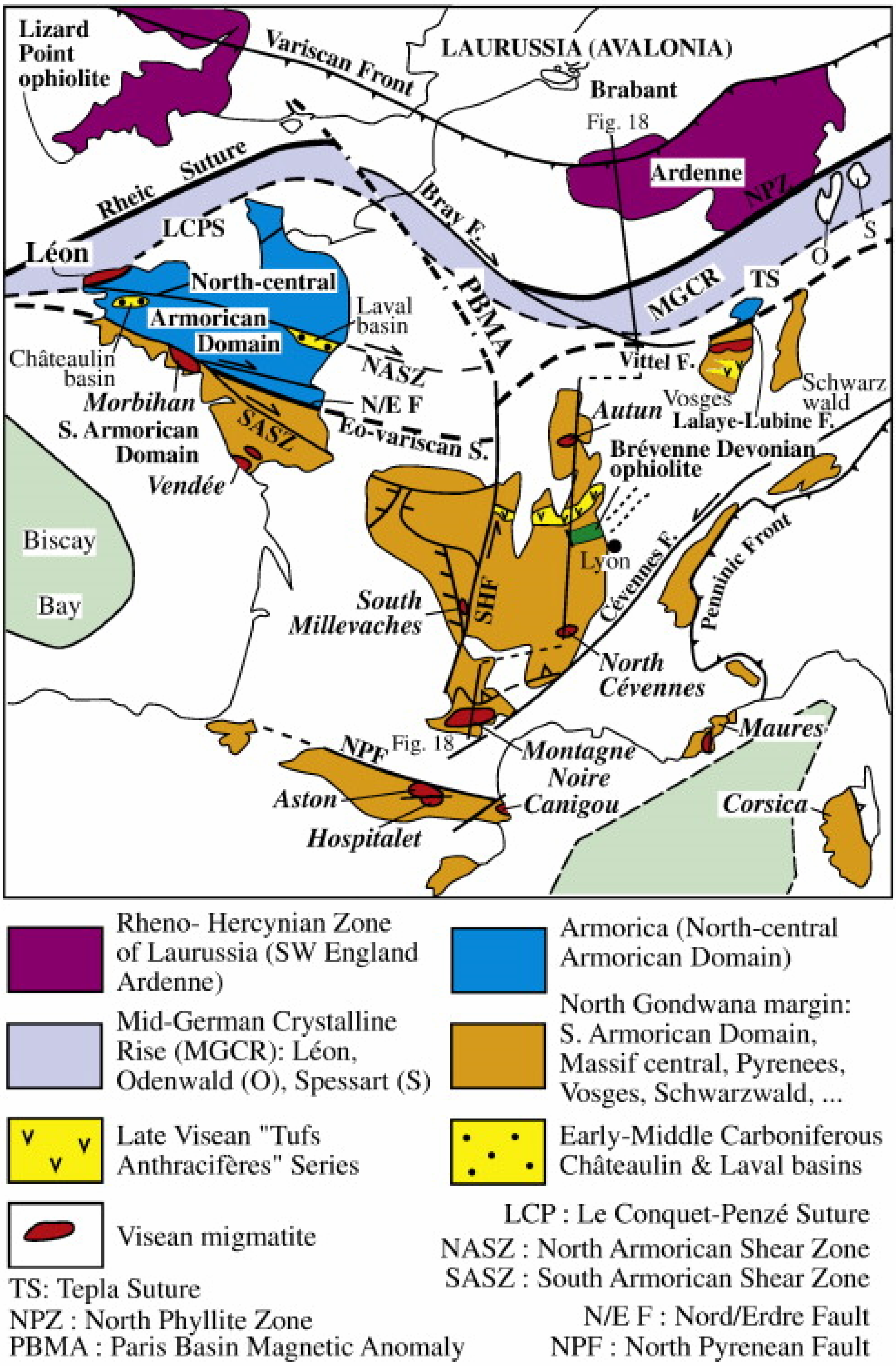

Fig. 17. : Tectonic map of the Variscan French massifs showing the zonation of the belt, and the widespread location of the Middle Carboniferous partial melting, Late Visean–Serpukhovian migmatites, and the Late Visean "Tufs anthracifères" series. MGCR: Mid-german crystalline rise interpreted as a microcontinent extending in the Léon in NW Massif Armoricain. In the MGCR, O: Odenwald, S: Spessart.

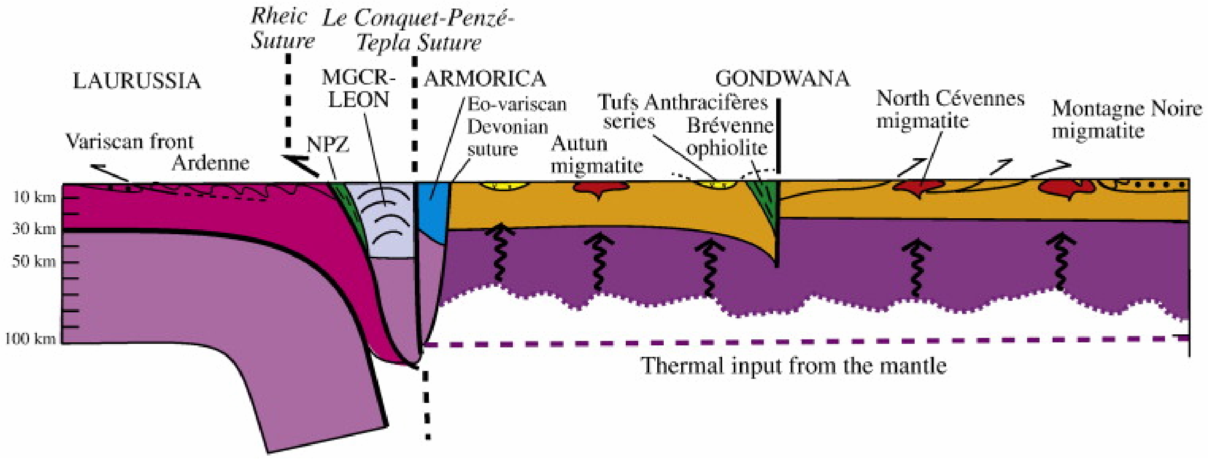

Fig. 18. : Lithosphere-scale interpretative cross-section of the French segment of the Variscan Belt from the Laurussian northern foreland up to the Gondwanian southern foreland during the Late Visean. In order to emphasize the Visean tectono-thermal events, younger granitoids have been omitted. In the French Massif Central, excepting the Eo-variscan suture, other Devonian features are not represented too. After the Early Carboniferous amalgamation of Laurussia, MGCG-Léon, and Gondwana continents was completed by south-directed subduction, the mantle lithosphere was thinned and heat transfer from the asthenosphere triggered the melting of the middle crust giving rise to intracustal convection and development of the "Tufs anthracifères" series, and anatectic granite–migmatitic complexes throughout the entire belt.